FABRICATION, DYNAMICS AND SELF-ASSEMBLY OF ANISOTROPIC COLLOIDAL PARTICLES

BY

ADAM JAMES DECONINCK

THESIS

Submitted in partial fulfillment of the requirements
for the degree of Master of Science in Materials Science and Engineering
in the Graduate College of the
University of Illinois at Urbana-Champaign, 2010

Urbana, Illinois

Master's Committee:

Professor Jennifer A. Lewis, Director of Research

Abstract

The self-assembly of colloidal particles into larger structures is of interest both scientifically and technologically. The range of possible structures that may be formed by isotropically-interacting spherical particles is narrow, encompassing only a few possibilities. To overcome this limitation, one can introduce one or more forms of anisotropy to the particles to guide their self-assembly.

In this work, we study the fabrication and behavior of polymeric microparticles that are chemically- and shape-anisotropic. Single-component, rod-shaped particles are fabricated by stop-flow lithography (SFL) using either hydrophobic and hydrophilic materials. SFL is also used to fabricate Janus particles that incorporate both chemistries within a single particle. The dynamical behavior and self-assembly of these rods are investigated using fluorescence and confocal microscopy over a range of different aspect ratios and environmental conditions. We also developed image processing algorithms to enable the quantitative analysis of these data, adapting standard particle identification and tracking techniques to the analysis of rod-shaped colloids. Finally, we demonstrated the fabrication of colloidal particles with branched and more complex morphologies, and briefly studied the self-assembly of these "patchy" particles.

To Leigh.

Acknowledgments

The completion of this work involved the participation of many talented scientists and engineers in addition to myself, and without their assistance I would still be sitting perplexed in the lab.

First of all I would like to thank my advisor, Professor Jennifer Lewis, whose contributions and support were essential at all stages of this project. Professor Jacinta Conrad and Dr. Robert Shepherd also provided essential assistance throughout my entire graduate career, contributing valuable knowledge and suggestions both in the lab and with my data analysis. I owe special thanks to my undergraduate assistants, Alissa Cote, Stephen Menke, Fatima Salazar, and Kundan Chaudhary, who collectively fabricated and imaged many thousands of interestingly-shaped particles and provided many helpful ideas. I had many helpful conversations with Scott Slimmer, who was also kind enough to proofread this document. I would also like to thank the rest of the Lewis Group for their help and support; in particular, Elizabeth Glogowski, Chris Hansen, John Vericella, David Lorang, Willie Wu, and Steve Kranz all contributed to expertise or assistance in this project. Special thanks also go to Jon Ekman of the Imaging Technology Group at the Beckman Institute, who assisted in acquiring many of the images used in the analysis of Janus assembly in Chapter 3 and is now enjoying sunny Florida.

My thanks and appreciation go to the University of Illinois, the Army Research Office, and the American Society for Engineering Education, who provided funding and support throughout my graduate career.

I would also like to convey my personal thanks to my friends and family, who reminded me that there is more to life than research. Mom, Dad and Brian were always there for me, and had to listen to me rant about frustrations in the lab far more often than I like to admit. Dr. Huaibin Zhang was kind enough to give me fascinating things to work on while I wasn't worrying about Janus particles, and Max, Steve, and Phil gave me games to play when I was done with that, too. Dorian, Moki and Tink were all true friends during rough times and deserve their own share of credit for the completion this work. And most of all I thank Leigh, without whom I would still be utterly lost, hiding in a lab. This is for you.

Table of Contents

List of Figures

List of Tables

Chapter 1

Introduction

As a class of materials, colloidal suspensions are of interest both in the study of self-assembly [1] and in applications such as photonic crystals [6, 7] and three-dimensional templates for tissue engineering scaffolds [8]. However, despite the broad interest in these materials, the range of possible structures accessible by the self-assembly of isotropically-interacting spherical colloids is relatively narrow. Due to the isotropic nature of colloidal interactions, there are only a few possibilities. When the interparticle interaction is purely repulsive, such as in a hard-core interaction, a stable, ordered face-centered-cubic crystal structure(Fig. 1.1(a)) with a volume fraction of 0.74 is formed. [9, 10] Alternatively, less well-ordered random close-packed configurations ($\phi \simeq 0.64$) may emerge. When the interparticle interaction is attractive, the particles may form an open, disordered "gel" structure (Fig 1.1(b)) with an essentially random arrangement and gap volumes which are potentially larger than the particle size. [11]

Many applications, such photonic crystals, would benefit from the availability of different kinds of self-assembled structures. [1] One way to address this need is to introduce colloidal particles that incorporate one or more forms of anisotropy, in which the interaction between two or more particles becomes non-uniform depending on their relative orientations. This anisotropy may be achieved by altering the shape of the particles, the chemical makeup of the particles, or some combination of the two.

In a 2007 article in *Nature Materials* [1], Glotzer and Solomon propose the system

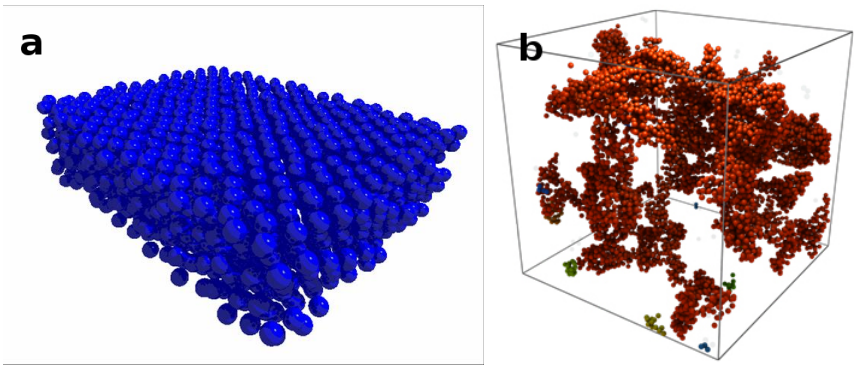

Figure 1.1: Spherical colloids with purely repulsive interactions assemble into (a) ordered crystal structures with fcc geometry, while spheres with attractive interactions may assemble into (b) open "gel" structures.

of anisotropy classification shown in Fig. 1.2. These anisotropy dimensions include shape-based dimensions such as aspect ratio, faceting, branching, shape gradient, and roughness (Fig. 1.2(B,C,E,G,H)), as well as dimensions based on the presence of multiple chemistries, such as surface coverage, pattern quantization, and chemical ordering (Fig. 1.2(A,D,G)). These dimensions do not necessarily represent an exhaustive classification of the types of anisotropy which are theoretically possible, but instead generalize from anisotropy types that have been observed in the recent literature. For example, rod-shaped or ellipsoidal particles of moderate aspect ratio have been fabricated by a wide variety of techniques including lithography [12] and the stretching of colloidal spheres [2]; branched tetrapods have been fabricated of gold [13], and CdTe [14]; and chemically patterned particles have been produced through microfluidic means [15] as well as by conventional photolithography. [16] This list of dimensions may therefore be seen as a useful framework for classification: by combining multiple dimensions, more complex types of particles may be designed (Fig. 1.3), or a complex particle may be classified in terms of which dimensions it includes. New forms of anisotropy may be identified as those which cannot be decomposed into dimensions already identified.

In this thesis, we develop techniques for the fabrication of colloids with geometric

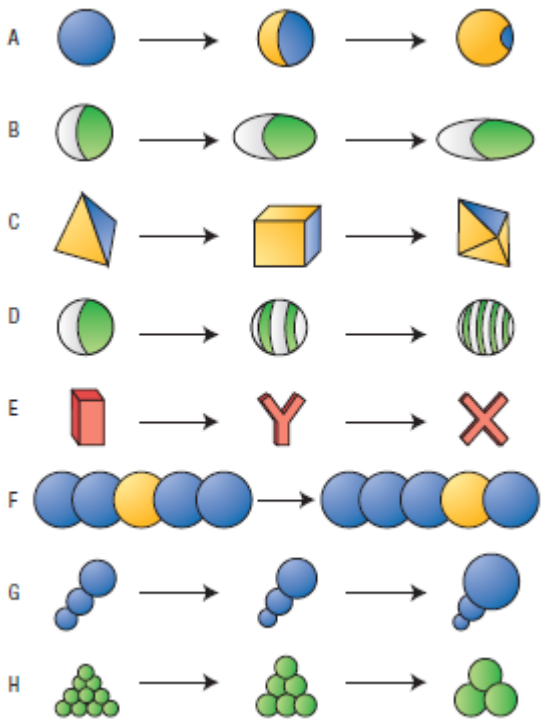

Figure 1.2: Anisotropy dimensions proposed by Glotzer and Solomon [1] to classify different forms of particle anisotropy.

and chemical anisotropy and initiate investigations of their dynamical behavior and self-assembly.

1.1 Thesis Scope

The aim of this work is to develop techniques for the fabrication and characterization of anisotropic colloids and to begin to explore their dynamical and self-assembly behavior. Fabrication is based on flow lithography techniques for producing polymeric particles [17, 4], and characterization is primarily based on fluorescence and confocal microscopy [18] and particle tracking. [19, 2] The systems used are based on a combination of a hydrophobic monomer (tri(methylol propane) triacrylate) and hydrophilic monomers (poly(ethylene glycol) diacrylate and 20-mol ethoxylated tri(methylol propane) triacrylate). Single-component particles are used to study the

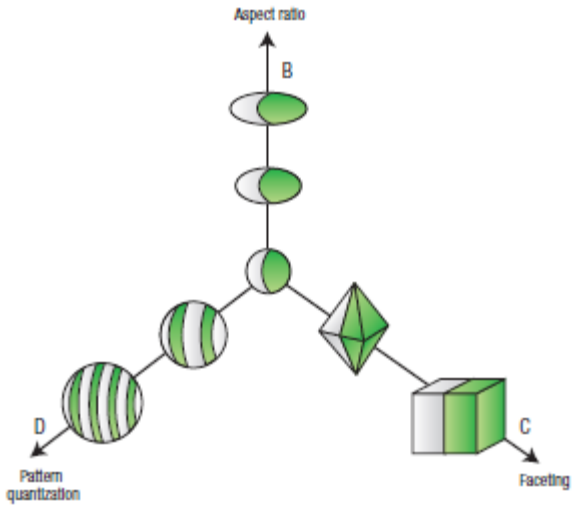

Figure 1.3: Multiple anisotropy dimensions may be combined to yield more complex forms. [1]

effects of geometry on dynamical behavior in isolation, while multiple-component particles introduce hydrophobic interactions that guide self-assembly. Particles are suspended in a variety of solvents to explore their interaction, including water, ethanol, dimethyl sulfoxide, isopropanol, and toluene.

1.2 Thesis Organization

Chapter 2 details algorithms and software developed in the course of this study to analyze microscopy images containing anisotropic colloids. Chapter 3 investigates the fabrication, behavior and self-assembly of simple rod-shaped colloids in both single-component and "Janus" forms, while Chapter 4 investigates colloids with more exotic geometries. The main conclusions are presented in Chapter 5. Appendix A details the Matlab implementation of the algorithms developed in Chapter 2.

Chapter 2

Computerized Tracking of Rod-Shaped Colloids

2.1 Introduction

Confocal laser scanning microscopy (CLSM) is a powerful technique for the study of three-dimensional structure in fluorescent materials. When applied to colloidal suspensions, CLSM allows the observation of individual particles and provides detailed data about the geometric configuration of the material. [18] This data alone can be used to derive a great deal of information about the material characteristics, such as the distribution of number of nearest neighbors and the pair distribution function (PDF). Repeated observations at regular intervals allow for dynamical measurements of parameters, such as the diffusion constant. [18, 19]

However, the production of useful 3D structural information requires more than just a high-resolution imaging technique: it also requires powerful computational analysis tools to translate image data into a list of particles and positions and calculate the physical characteristics of interest from these positions. In addition, the behavior of non-spherical colloids is governed not only by the relative positions of the particles but also their orientations. Developing an understanding of anisotropic colloids therefore calls for the development of image processing techniques for the extraction and analysis of structural data from microscopy images.

In Section 2.2, we describe techniques from the literature for the tracking of spherical and ellipsoidal colloids. Section 2.3 develops an algorithm for the identification and tracking of rod-like colloids fabricated by stop-flow lithography, and Section 2.4

demonstrates the use of this algorithm to track diffusing and self-assembled particles. Appendix A describes the implementation in Matlab of the algorithm developed in Section 2.3.

2.2 Background

2.2.1 Tracking of Spherical Colloids

In a 1996 paper in the *Journal of Colloid and Interface Science* [19], John Crocker and David Grier outline a five-stage procedure for the tracking of spherical colloidal particles. This algorithm was implemented in IDL [20] and has become the standard for carrying out 3D tracking of spherical particles. It has since been ported to other environments such as Matlab [21, 22] and LabView [23] which are also commonly used in the scientific community.

Image Restoration

CLSM imaging of colloidal suspensions may introduce camera noise and geometric distortions that lead to images that do not accurately describe the geometry of the suspension. These effects can be compensated for by applying a spatial band-pass filter to the image, A. This filter is composed of two parts.

The first part is a boxcar average [24] over a region of extent $2w + 1$, where w is an integer larger than a single sphere's apparent radius in pixels, but smaller than an intersphere separation:

$$A_w(x, y) = \frac{1}{(2w+1)^2} \sum_{i,j=-w}^{w} A(x+i, y+j) \tag{2.1}$$

The second part is a convolution of the image with a Gaussian surface of revolution with half-width $\lambda_n \approx 1$ pixel:

$$A_{\lambda_n}(x,y) = \frac{1}{B} \sum_{i,j=-w}^{w} A(x+i, y+j) \exp\left(-\frac{i^2+j^2}{4\lambda_n^2}\right) \tag{2.2}$$

with normalization B = $[\sum_{i=-w}^{w} \exp -(i^2/4\lambda_n^2)]^2$.

These two filters can be applied simultaneously in a single step using the convolution kernel

$$K(i,j) = \frac{1}{K_0}\left[\frac{1}{B}\exp\left(-\frac{i^2+j^2}{4\lambda_n^2}\right) - \frac{1}{(2w+1)^2}\right] \tag{2.3}$$

The normalization constant $K_0 = 1/B[\sum_{i=-w}^{w} \exp -(i^2/2\lambda_n^2)] - (B/(2w+1)^2)$ facilitates comparison among images filtered with different values of w.

Locating Particles

Particles are located by identifying local brightness maxima within an image. A pixel is identified as a position candidate if no other pixel within a distance w is brighter, where w is the same value used in the filtering step. This was implemented by Crocker and Grier using a gray-scale dilation operation. [24]

Refining Location Estimates

Having located a brightness maximum at coordinates (x, y) which is presumably near a sphere's geometric center at (x_0, y_0), additional refinements are possible which may achieve sub-pixel accuracy. An offset (ϵ_x, ϵ_y) is calculated according to:

$$\begin{pmatrix} \epsilon_x \\ \epsilon_y \end{pmatrix} = \frac{1}{m_0} \sum_{i^2+j^2 \leq w^2} \begin{pmatrix} i \\ j \end{pmatrix} A(x+i, y+j) \tag{2.4}$$

Here, $m_0 = \sum_{i^2+y^2 \leq w^2} A(x+i, y+j)$ is the integrated brightness of the sphere's image. The refined location estimate is then $(x_0, y_0) = (x + \epsilon_x, y + \epsilon_y)$. If either $|\epsilon_x|$ or $|\epsilon_y|$ exceeds 0.5, the candidate centroid location can be moved and the refinement recalculated.

Noise Discrimination and Tracking in Depth

During the centroid refinement calculations, two moments of each sphere image's brightness distribution are calculated:

$$m_0 = \sum_{i^2+y^2 \leq w^2} A(x+i, y+j) \tag{2.5}$$

$$m_2 = \frac{1}{m_0} \sum_{i^2+j^2 \leq w^2} (i^2 + j^2) A(x+i, y+j) \tag{2.6}$$

where (x, y) are the refined centroid locations. The distribution of the (m_0, m_2) data reflects the sphere's positions along the direction normal to the imaging plane, and a control experiment using a monolayer of particles is used to calibrate this data.

Linking Locations Into Trajectories

Having located the colloidal particles in a sequence of video images, it is possible to match particle locations in each image with corresponding locations in later images to

produce trajectories. This requires determining which particle location in a given image most likely corresponds to the same particle in the preceding image. The tracking of multiple particles requires that we seek the most probable set of N identifications between N locations in two consecutive images. If the particles are indistinguishable (as for monodisperse colloidal particles), this likelihood can be estimated only using relative proximity.

The probability that a single Brownian particle will diffuse a distance δ in the plane in time τ is

$$P(\delta|\tau) = \frac{1}{4\pi D\tau} \exp\left(-\frac{\delta^2}{4D\tau}\right) \tag{2.7}$$

where D is the particle's self-diffusion coefficient. For an ensemble of N noninteracting identical particles, the corresponding probability distribution is the product of the single-particle results:

$$P(\delta_i|\tau) = \left(\frac{1}{4\pi D\tau}\right)^N \exp\left(-\sum_{i=1}^{N} \frac{\delta_i^2}{4D\tau}\right) \tag{2.8}$$

Each label assignment can be thought of as a bond drawn between a pair of particles in consecutive frames. $P(\delta_i|\tau)$ is calculated for all possible combinations which represent a displacement below some characteristic length scale L, selected by the user based on the experimental conditions.

2.2.2 Rod Tracking

While the algorithm by Crocker and Grier is used widely for tracking spherical particles, it cannot deal with particles that have an anisotropic shape and some orientation.

To begin to deal with simple anisotropy, Mohraz and Solomon developed an algorithm for tracking ellipsoidal colloidal rods based on the spherical tracking algorithm. [2, 25]

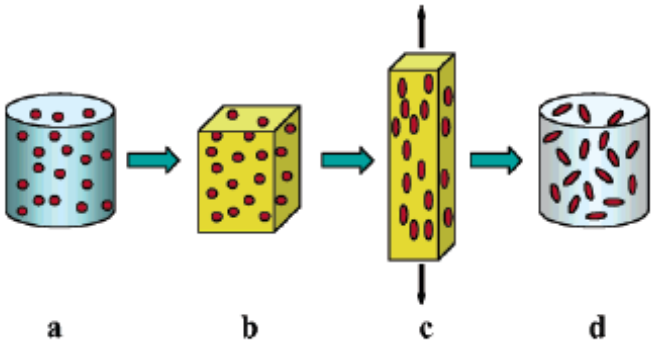

Figure 2.1: (a) Synthesis of PMMA-g-PDMS spheres, (b) curing of the PDMS matrix, (c) uniaxial deformation, and (d) rod harvesting. [2]

To provide experimental data for the development of this algorithm, a suspension of ellipsoidal rods was fabricated (see Figure 2.1). Poly(methyl methacrylate)-g-poly(dimethylsiloxane) (PMMA-g-PDMS) fluorescent colloidal spheres were synthesized, and then suspended in a polymerizable liquid silanol-terminated PDMS. The film then cured to form a solid matrix. This matrix was then heated above the glass transition temperature of PMMA-g-PDMS and subjected to uniaxial stretching, then cooled while still deformed. The rods were then harvested from the elastic film by chemical degradation, and transferred to a cyclohexyl bromide (CXB) solution. The suspension of the colloidal rods was then visualized via CLSM, and subjected to a three-stage image processing algorithm to determine the position and orientation of each rod.

Image restoration

To correct for imaging distortions and local noise, pixels are convoluted with neighbors found within a local distance w using a Gaussian function, where w is of the order of the rod half-width. The resulting pixel intensity $A(x, y, z)$ is

$$A(x,y,z) = \frac{1}{B(x,y,z)} \sum_{i,k,j=-w}^{w} A(x+i, y+j, z+k) \exp\left(-\frac{i^2+j^2+k^2}{6\lambda^2}\right) \qquad (2.9)$$

where B is a normalization constant and λ is defined to be 1 for these experiments.

Rod Backbone Identification

Rod backbones are identified using a local line maximum criterion (Figure 2.2). Each pixel is compared with its immediate neighbors in all directions along lines with length $2w+1$. If a candidate pixel is found to be the brightest point on more than a critical fraction of these lines (typically 70%), it is considered to be a backbone pixel. Backbone pixels are then grouped together via cluster analysis to form rod backbones. Figure 2.3(a) shows both the original fluorescence image and identified backbones for PMMA-g-PDMS rods embedded in a stretched PDMS film (Figure 2.1(c)), and Figure 2.3(b) shows the same images for freely-suspended rods.

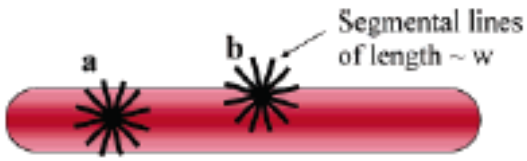

Figure 2.2: To identify candidate backbone pixels, each pixel is compared in its immediate neighbors in a local line maximum criterion.

Orientation and Centroid Calculation

Once the backbone pixels for a given rod have been identified, the position and orientation of each rod may be determined based on these pixels' locations. Each rod's geometric configuration can be completely specified by three positional coordinates, x, y and z, and two orientational coordinates θ and ϕ, as shown in Figure 2.4.

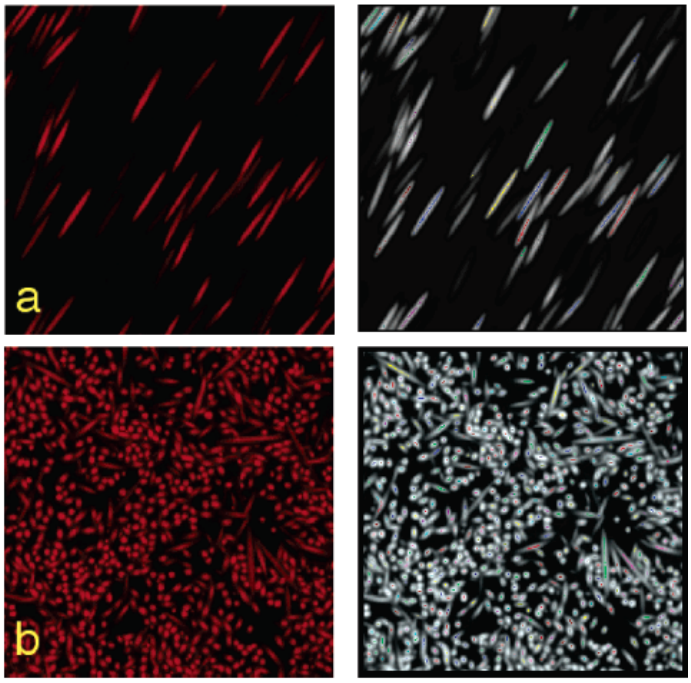

Figure 2.3: Rod backbone assignments in (a) a stretched film and (b) a sediment structure.

The rod's center-of-mass position may be calculated straightforwardly based on a simple average over the positions of the backbone pixels. In Equations 2.10–2.12, $r_{0,i}$ represents the center-of-mass of coordinate r for rod i. S_i is the number of identified backbone pixels associated with that rod, and s is the index variable summing over that set.

$$x_{0,i} = \frac{1}{S_i} \sum_{s}^{S_i} x_{s,i} \tag{2.10}$$

$$y_{0,i} = \frac{1}{S_i} \sum_{s}^{S_i} y_{s,i} \tag{2.11}$$

$$z_{0,i} = \frac{1}{S_i} \sum_{s}^{S_i} z_{s,i} \tag{2.12}$$

Calculating orientation is somewhat more complex. First, for each dimension r, the quantity $| < l_r^2 >^{1/2} |$ is calculated (Equations 2.13–2.15). Geometrically, this is

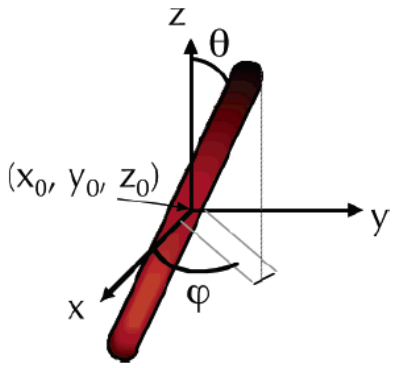

Figure 2.4: Positional and orientational coordinates for colloidal rods. [2]

the size of the projection of the rod's length onto the axis r. Once these dimensions have been calculated, the angles θ and ϕ may be determined according to 2.16 and 2.17, respectively.

$$| < l_x^2 >_i^{1/2} | = \left[\frac{1}{S_i} \sum_s^{S_i} (x_{s,i} - x_{0,i})^2 \right]^{1/2} \tag{2.13}$$

$$| < l_y^2 >_i^{1/2} | = \left[\frac{1}{S_i} \sum_s^{S_i} (y_{s,i} - y_{0,i})^2 \right]^{1/2} \tag{2.14}$$

$$| < l_z^2 >_i^{1/2} | = \left[\frac{1}{S_i} \sum_s^{S_i} (z_{s,i} - z_{0,i})^2 \right]^{1/2} \tag{2.15}$$

$$\theta_i = \cos^{-1} \left(\frac{< l_z^2 >_i^{1/2}}{< l^2 >_i^{1/2}} \right) \tag{2.16}$$

$$\phi_i = \tan^{-1} \left(\frac{< l_y^2 >_i^{1/2}}{< l_x^2 >_i^{1/2}} \right) \tag{2.17}$$

2.3 Tracking Algorithm

Our method for locating and tracking rods produced by stop-flow lithography (SFL) draws heavily from that published by Mohraz and Solomon for tracking PMMA

rods. [2]. While this algorithm performs very well for a restricted class of elliptical rods, it fails in cases where the particle cross-section is not circular, so that points near the particle backbone are not guaranteed to produce higher intensities than their immediate neighbors. This is the case for our "rods" produced by SFL, in which the thickness of the rods is relatively uniform due to the fabrication geometry. These particles have correspondingly flat fluorescence profiles and require a more complex analysis to calculate a "backbone".

We have developed an algorithm for processing 2D and 3D CLSM data of fluorescent SFL rods to produce position and orientation data. Starting from raw CLSM images, this algorithm can be divided into five phases, including (i) image cleanup; (ii) segmentation; (iii) skeletonization; (iv) position calculation; and (v) particle tracking over a time series.

A note on terminology: the algorithm described below is identical for both 2D and 3D images, as all operations are defined for both cases and used identically. However, where the individual elements of 2D images are referred to as pixels, the elements of 3D images are generally referred to as voxels. For simplicity, all such elements are referred to as pixels in the explanation below.

2.3.1 Image Cleanup

For any given set of images, two different image cleanup techniques were used for test images, and the best result was used for the entire set.

The first method was a spatial band-pass filter, described in Section 2.2.1 and implemented in Matlab by Blair and Dufrense [21]. This filter takes two parameters, the characteristic scale of image noise, generally equal to one pixel, and the typical particle size. This approach generally works well, but has difficulty in images with multi-pixel noise.

While the band-pass performed well on some images, many experiments produced

data with noise or extraneous features that did not easily yield to the bandpass operation. This issue can be attributed to the fact that SFL fabrication produces solutions that contain some amount of residual fluorescent monomer, which can not always be removed effectively. A second image cleanup technique was therefore devised using morphological operations to better suppress non-particle features.

This method may be divided into five steps. First, the image is run through a morphological top-hat transform. [24] This transform is used to compensate for the effects of uneven illumination in the image. The image is then thresholded to produce a binary image, where the background is black and the fluorescent features are white. The threshold is selected such that pixels that are part of the particle volume are never assigned to the background; Otsu's criterion was found to be reliable for this. [26] Next, a binary opening is applied with an isotropic structuring element to suppress small features. The size of the structuring element was selected manually by the user based on performance in test images, but a reliable choice was found to be a diameter roughly equal to half the width of the typical rod.

At this point a binary image has been produced that suppresses most non-particle features, but morphological image operations are not guaranteed to preserve shape and orientation of image features. To retain the noise suppression, but regain the original shape, we perform one additional morphological dilation using the same structuring element to guarantee that the foreground regions fully overlap with the rods. Finally, we perform a binary AND between the result and the original image. This is effectively equivalent to using the result of our morphological operations as a mask on the original, suppressing all pixels that are marked as background.

2.3.2 Segmentation

The next step of the algorithm is image segmentation, in which individual particles are identified and each pixel in the image is assigned to either a specific particle or

the background.

First, the image is thresholded to produce a binary image, with a threshold selected such that all pixels that are part of the rods are assigned to the foreground. Again, this may generally be accomplished through the use of Otsu's criterion. [26]

Second, the Euclidean distance transform is calculated. [27] In this step, each foreground pixel is assigned a number which gives the distance between this pixel and the nearest background pixel. In this algorithm, the distance measure used is simple Euclidean distance, calculated center-to-center between this pixel and the closest background pixel. Alternative distance measures such as the "chessboard" measure may also be used to speed up computation, but these measures were found to negatively impact segmentation. To prepare the image for watershed segmentation, the distance transform is transformed such that all distances are made negative, while the background remains at a flat zero. An h-minima transform is applied to remove small local minima due to noise in the image. [24]

The primary segmentation step is the *watershed transform*. [28] In this transform, a gray-level image is viewed as a topographic relief map where the pixel values represent altitude. A drop of water falling on a relief surface will run down to a local minimum, and many drops will fill any local minima present until the basins meet. Implementations of the watershed transform use this concept to calculate the boundaries between catchment basins, fully segmenting the image. The number of basins is calculated either by using local minima in the image, or by pre-assigning a set of markers. In our algorithm, we generally use the Matlab implementation of `watershed` which uses the local minima method. A local-minima based watershed transform may result in some over-segmentation, but this effect can be mitigated by using the h-minima transform to remove artifacts. While a marker-based technique would avoid this issue, it is much more cumbersome when a large number of images must be processed.

`watershed` outputs an image that labels each pixel according to a region ID number, and labels both background and foreground pixels with these regions. To restrict these labels so that the background is labeled separately, all watershed pixels that correspond to background-valued pixels in the thresholded image are assigned a label number of zero.

2.3.3 Skeletonization

Once we have identified which image pixels belong to each particle, we need to put this data into a form from which reliable position and orientation information can be calculated. While it is tempting to simply calculate the centroid and associated moments from the raw pixel data, this can be problematic when working with time-series data due to boundary noise. Consider a single foreground pixel belonging to an identified particle that is experimentally constrained to be stationary, and which is adjacent to a background pixel because it is on the edge of the identified region. In the next image in the time series, this pixel's intensity is reduced and it is identified as a background pixel. If we calculated particle position as the average of all the identified pixels, this would result in the calculated position changing, even if the particle did not physically move. The next frame after that, it may be re-identified as a foreground pixel. While the effect is small, experimental conditions may magnify these effects and produce appreciable fluctuations in the position and orientation. One way to avoid this problem is to calculate a particle "skeleton", which is less sensitive to this form of noise. [24]

For a rod, we calculate a backbone very similar to the backbone calculated in the Mohraz-Solomon algorithm. However, because of the flat fluorescence profile of SFL rods, we cannot use the fluorescence intensity maximum to identify backbone pixels. Instead, we calculate the backbone position with respect to the particle geometry. For each particle, we isolate its pixels from the environment, i.e., generate a new

image containing only this particle. We then calculate the distance transform to allow identification of pixels that are closest to the geometric backbone. These are identified by applying a "percentile threshold", in which all pixels that fall below a given percentile in the distribution are reassigned as background pixels. The correct value of this threshold is determined by the analysis of a trial image from the image set, and typically falls in the 85–95% range.

2.3.4 Calculation of Position and Orientation

Position and orientation are calculated from particle backbones in an identical fashion as in Mohraz and Solomon [2]; see Section 2.2.2 for details.

2.3.5 Time-Series Tracking

Building a set of particle trajectories from the frame-by-frame list of particle positions was accomplished using the Blair and Dufrense implementation [21] of the tracking procedure developed by Crocker and Grier [19] and outlined in Section 2.2.1, with the orientation information ignored for the purposes of tracking and simply "carried along" with the corresponding position data.

2.4 Results and Discussion

2.4.1 Dynamics

Poly(ethylene glycol) diacrylate rods with dimensions $5 \times 3 \times 3$ μm were fabricated via SFL and suspended in water. Their diffusion was observed as described in Section 3.3.6 with an image collection rate of 2 frames per second. The resulting image sequence was imported into Matlab, and tracking was carried out using the scripts outlined in Appendix A. Noise reduction was carried out using a band-pass filter

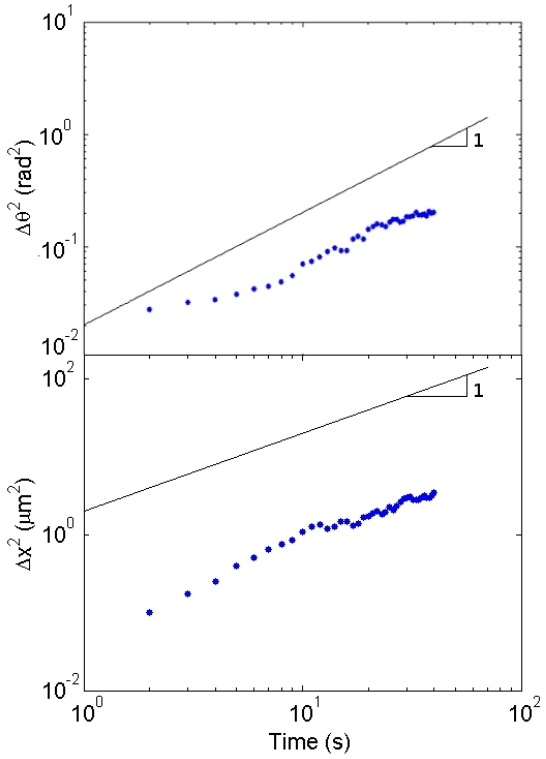

Figure 2.5: Translational and rotational diffusion results for 12 μm SFL-fabricated rods.

with noise and particle dimensions of 1 pixel and 30 pixels respectively. Watershed segmentation was carried out using a `height` parameter of 1, and skeletonization was performed using a percentile filter of 0.95. The maximum allowable displacement between subsequent frames, `maxdisp`, was set to be 15 pixels. Finally, the MSD of translational and rotational diffusion were calculated to prodice the results in Figure 2.5. A series of experiments was carried out to study the effect of rod size and aspect ratio on 2D diffusion, as detailed later in Section 3.4.3.

2.4.2 Structure

Janus rods were fabricated with hydrophilic and hydrophobic components to induce self-assembly. In Figure 2.6, the results of a 2D image analysis for aligned Janus

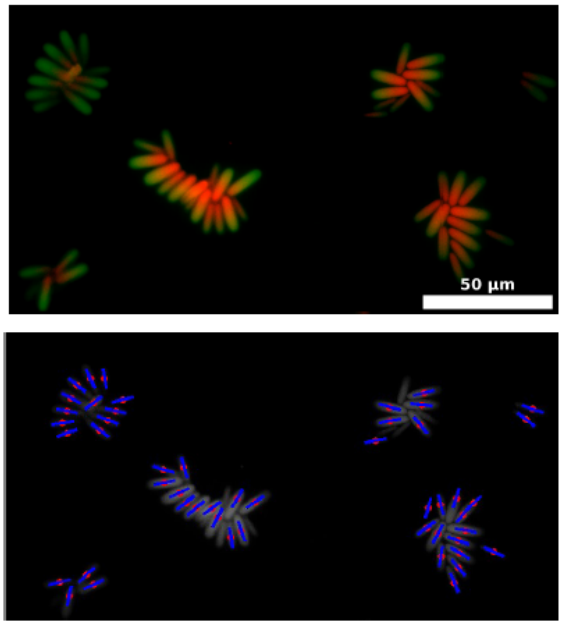

Figure 2.6: Janus rods were observed to assemble in micelle-like clusters (top), and the particle centers-of-mass and orientations are tracked (bottom).

clusters are shown. This analysis is carried out using the morphological clean-up process with a top-hat structuring element of radius 40 pixels, a opening structuring element of radius 2, and the default thresholding method. Segmentation was carried out using a `height` parameter of 4, and skeletonization used a percentile filter of 0.9. A `cutoff` value of 50 was used in the position calculation step.

A series of experiments was carried out to study the self-assembly of Janus rods by varying the solvent conditions for assembly and rod aspect ratio. Orientational ordering and number of nearest neighbors are calculated across this experiment series, and the results are detailed in Section 3.4.4.

Chapter 3

Assembly and Dynamics of Rod-Shaped Colloids

3.1 Introduction

When one is first presented with the different dimensions of anisotropy proposed by Glotzer and Solomon (Figure 1.2, [1]), the potential variety of particle types can be overwhelming. It is therefore useful to begin by studying particles engineered with only one or two of these anisotropy dimensions. To this end, we first focused on particles that vary only in the dimension of aspect ratio, i.e., colloidal rods. In this chapter, we present the fabrication of both single-component and Janus rods by stop-flow lithography, the study of rod diffusion by particle tracking, and the basics of self-assembly for Janus rods in different solvents.

In Section 3.2, the flow lithography technique for particle microfabrication is described in detail. Section 3.3 describes the experimental procedure for the fabrication of microfluidic devices for stop-flow lithography, the fabrication of single-component and Janus rods, particle collection and purification, and the observation of rod suspensions by fluorescence and confocal microscopy. Section 3.4.1 describes the results of trials of different rod collection techniques, while Section 3.4.2 describes observations of surface interactions between colloidal rods and various surfaces. Section 3.4.3 shows the results of translational and rotational diffusion measurements, and Section 3.4.4 describes experiments on the self-assembly of Janus rods.

3.2 Background

3.2.1 Continuous-Flow Lithography

One method for the fabrication of structured particles that has undergone active development in recent years is *flow lithography*, a technique developed by the Doyle Group at the Massachusetts Institute of Technology which combines microfluidics with ultraviolet (UV) lithography. Flow lithography may be carried out in either a continuous- or stop-flow for the photopolymerization step.

In a typical continuous-flow lithography (CFL) experiment, [17], a polydimethylsiloxane (PDMS) microfluidic device is constructed that contains a simple straight microchannel with cross-sectional dimensions between 5-400 μm. As a feedstock material, a fast-photocuring low-viscosity liquid, typically a photocurable monomer solution, is used. The device is placed on a microscope that includes a UV illumination source that may be reversed through the optical path (i.e., emitted at the objective lens) and a fast electronic shutter. A typical example would be a conventional fluorescence microscope with a mercury lamp. A transparency photomask defining the particle geometry is placed at the microscope field stop to mask the UV beam. To fabricate particles, the photocurable liquid is pumped at a constant rate through the microchannel, and the microchannel is oriented parallel to the microscope's focal plane. The microscope objective is focused on a plane inside the channel volume, and the electronic shutter is opened at intervals. If the UV light is intense enough and the liquid is moving at a slow enough speed, the UV-exposed region will cure into one or more solid particles. The microchannel flow carries these particles out of the "active region", and then provides fresh unpolymerized material.

The particle geometry is defined by a combination of the photomask and the microchannel geometry. The two-dimensional cross-section is determined by the shape of the UV beam at its intersection with the microchannel, and the particle height

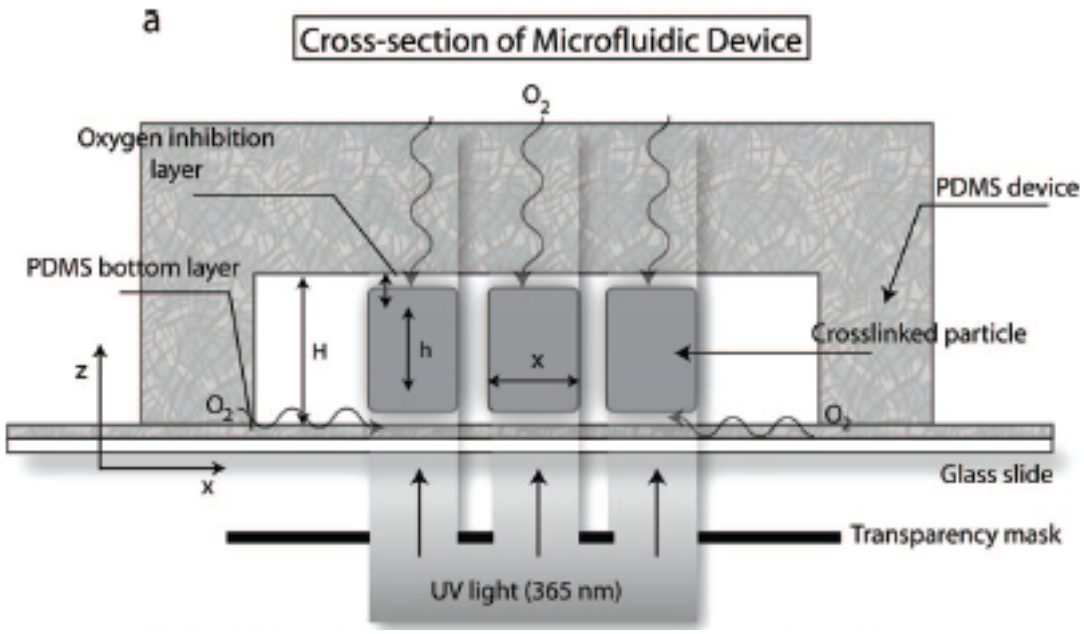

Figure 3.1: Photopolymerization is inhibited at the channel walls due to the presence of a layer dissolved oxygen, which has diffused into the channel due through the oxygen-permeable PDMS. [3]

is defined by the height of the microchannel. The upper and lower surfaces of the particles are flat, as they conform to the upper and lower microchannel surfaces, so that the particle geometry is a 3D extrusion of the photomask. Friction or sticking with these top and bottom surfaces are prevented when PDMS is used as the channel material and a hydrogel monomer is used as the feedstock, because hydrogel curing is inhibited by the presence of oxygen and PDMS is oxygen permeable. This results in the formation of an "inhibition layer" of dissolved oxygen along the internal surfaces of the channel where the liquid will not cure, preserving the mobility of the particles (see Figure 3.1). [3] This layer is typically a few microns thick, depending on details of the channel construction. The resolution and quality of the 2D pattern is affected by the quality of focus, the resolution of the mask, and the magnification and numerical aperture of the objective lens.

3.2.2 Stop-Flow Lithography

In *stop-flow lithography* (SFL), the cure-during-flow procedure in continuous flow lithography is replaced with a flow-stop-cure cycle in which the microchannel flow is allowed to come to a halt before UV exposure. (See Figure 3.2 for an experimental schematic.) This change allows for a substantial improvement in both fabrication resolution and throughput. [4]

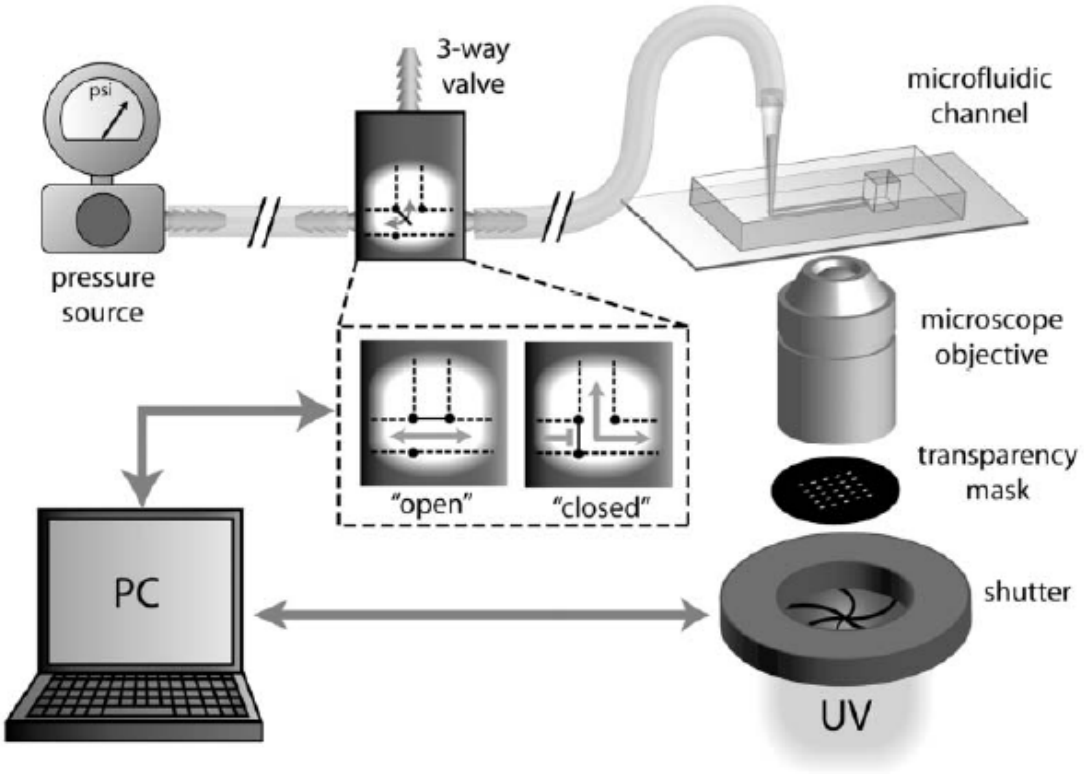

Figure 3.2: In a stop-flow lithography experiment, gas pressure is used to drive the flow of the photocurable solution. The flow is stopped at intervals using a three-way valve to divert the pressure, after which particles are produced via UV photopolymerization, carried out using an electronic shutter to actuate the UV exposure and a transparency mask to define the particle geometry. The valve and the shutter are synchronized by computer control; the pressure source may also be optionally controlled using the PC. [4]

First, resolution is improved because stopping the microchannel flow minimizes the effect of polymerization "smearing", which distorts the shape of the resulting

particles. When flowing monomer solution is exposed to UV light for a finite time, any monomer which occupies the exposed volume during that time begins to undergo photo-polymerization. Some of the solution will flow out of this region during this time and be replaced by additional solution from up-stream. This results in a particle which is "smeared" or "stretched" along the direction of flow and does not precisely reproduce the shape defined on the mask. When flow is stopped, this effect is minimized, and the only limitations imposed on the resolution are due to the optical system, the mask resolution, and materials constraints.

Second, throughput is greatly increased because higher rates of flow may be used during the periods when pressure is applied. In continuous-flow lithography, the rate of flow must be kept relatively slow in order to to allow curing to take place at all. Once particles have cured, no additional exposure step may take place until this flow has carried the particles out of the exposure region and fresh monomer has been supplied to carry out another cure step. In SFL, the rate of flow between exposure steps may be arbitrarily high as the cure step is carried out when the flow is stopped. When the cure step is finished in SFL, a high pressure is applied to quickly clear the exposure region, followed by a short pause to allow the fluid to stop flowing. This procedure has allowed fabrication rates as high as 10^5 particles min^{-1}. [4]

It is important to note that the advantage in throughput is reduced somewhat when the experiment design necessitates a long pause step after the flow. The length of this pause step is dependent on the fluid viscosity, but especially on the response time of the PDMS device. When a high pressure is applied to elastic PDMS microchannel, the walls of the channel deform to allow it to expand. Removing that pressure, as in SFL, produces a "squeeze flow" phenomenon in which the relaxation of the device walls generates fluid flow within the channel. The cure step cannot take place until this flow has ceased. This response time may be given as

$$\tau_r \sim \frac{\mu L^2 W}{E H^3} \tag{3.1}$$

where μ is the liquid viscosity, L is the channel length, W is the channel width, H is the channel height and E is the elastic modulus of PDMS. Note that this response time is not dependent on the input pressure, so that relatively high flow rates may be used without affecting the length of the pause step. However, this scaling becomes pressure-dependent and more complicated when the deformation in channel height Δh is comparable to H. [4]

3.2.3 Multiple-Component Fabrication

Polymeric particles consisting of multiple components of different chemistries may be produced by taking advantage of laminar flow in the device. In the laminar flow regime, several different streams may flow in parallel through the same microchannel without turbulence and with mixing limited to that caused by diffusion. [29] Diffusion alone will produce very little mixing, so that a sharp boundary between two streams may spread only a few microns over millimeters of linear flow. [30] The result is a multiple-stream microchannel flow in which multiple materials co-exist and are geometrically distinct.

If each co-flowing stream is made up of a photopolymerizable solution with similar curing kinetics, one may perform flow lithography using a mask which illuminates several streams at once in order to produce particles that contain geometrically distinct regions of different chemical makeup. A simple case is demonstrated in Dendukuri *et al.* [4] for SFL, in which dyed and un-dyed PEGDA solutions are cured in the laminar flow regime to produce particles whose fluorescence is confined to one part of the particle. Fabrication of amphiphilic microparticles containing both hydrophobic and hydrophilic materials is demonstrated by Dendukuri in *Langmuir* [31], and par-

ticles that incorporate biomolecule probes and lithographically-defined "barcodes" in different regions are fabricated by Pregibon *et al.* in a 2007 *Science* paper. [32]

3.3 Experimental Procedure

Colloidal rods were fabricated by stop-flow lithography (SFL), as described in Section 3.2.2 using hydrophobic and hydrophilic monomer solutions.

3.3.1 Microchannel Device Fabrication

Particle fabrication was carried out in three-input Y-junction microchannel devices (Figure 3.3). The primary channel of these devices had a typical height of 7 μm, width of 200 μm, and length of 3000-5000 μm. These dimensions were selected to facilitate the fabrication of large numbers of particles with small size in all dimensions: the low height facilitated small-particle fabrication by limiting the height of the particles, while the comparatively large width allowed many particles to be fabricated simultaneously. Multiple inputs were included to allow up to three monomer streams to be simultaneously flowed with a single exit point for collecting particles.

Photoresist Masters

Positive-relief photoresist master templates (or "masters") were fabricated by UV photolithography. A thin film of SU-8 2007 photoresist (Microchem) was laid down on a clean Si wafer by spin-coating at 3000 rpm to produce a 7 μm layer. Next, a "soft bake" was carried out by heating the wafer on a hot plate at 120°C for five minutes to evaporate the photoresist solvent. The device features were patterned by exposing the photoresist to UV light from a 300 W lamp for 40 s through a photomask defining the device design (Figure 3.3). A "hard bake" step was then carried out by heating the wafer at 120°$C$for ten minutes, to cure the photoresist in the exposed areas. Finally,

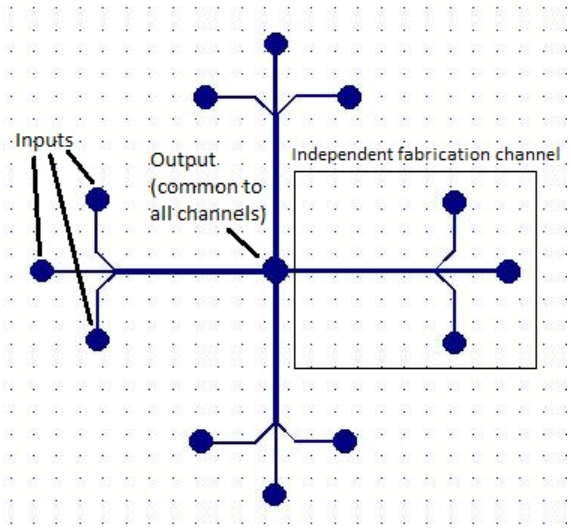

Figure 3.3: Photomask used in the exposure step of the photoresist master fabrication. Four fabrication microchannels, each containing three inputs, are arranged so that they share a common output. The channels are arranged thus so that the particle samples fabricated in multiple experiments may be combined to increase the volume of the combined sample. This is desirable due to the difficulties with collecting and processing particles with high yield (see Section 3.3.5 and 3.4.1).

the wafer was immersed in SU-8 developer (Microchem) and agitated for two minutes to remove the unexposed photoresist, then rinsed with isopropyl alcohol (IPA).

After fabrication, photoresist masters were subjected to a fluorinated silane vapor coating to inhibit adhesion between the SU-8 template and the elastomer to be cast. Masters were placed in a small desiccator (Fisher Scientific) along with an open container of (tridecafluoro-1,1,2,2-tetrahydrooctyl) trichlorosilane ("fluorosilane", Gelest, Inc.) This desiccator's vacuum port was then connected to a single-stage vacuum pump (Fisher Scientific) and evacuated for two hours to produce a silane coating.

Elastomer Device Construction

Microchannel devices were constructed from polydimethylsiloxane (PDMS, Dow Corning, Sylgard 184). PDMS elastomer and curing agent were mixed at a ratio of 10:1 by weight and poured over the photoresist master in a petri dish to a depth of about

2 mm. PDMS was also spun-coat onto a 48 x 60 mm #1 cover-slip (Gold Seal) to form the substrate for the device. Both of these were then baked at 65 $^{\circ}C$ for six hours or more to cure the PDMS.

Once the PDMS was fully cured, a razor blade was used to carefully cut out a section which encompassed some or all of the microchannels defined on the photoresist master. This section was then peeled up from the master, resulting in a block of PDMS with negative features defining the tops and sides of the microchannels. For each microchannel, three small holes ($\sim$0.5 mm) were punched at each entrance using a syringe press, and a larger hole ($\sim$3 mm) was punched at the exit using a biopsy punch.

Both the PDMS block defining the channels and the PDMS-coated glass substrate were rinsed with deionized water and IPA. Following this, small particles were removed by first laying down and then peeling up Scotch Magic brand transparent tape. Each section was then placed below a UV light-emitting tube lamp with the channel surface facing the lamp and exposed to UV light for ten minutes to promote PDMS-PDMS adhesion. After UV exposure, the channels and the substrate were then firmly pressed together with the channel surface of the top block against the PDMS-coated surface of the substrate. The resulting device was then baked at 100 $^{\circ}C$ for one hour to promote device bonding.

3.3.2 Photocurable Solutions

The hydrophobic solution was composed of 95 vol% tri(methylol propane) triacrylate (TMPTA, Sartomer) and 5 vol% Darocur 1173 photoinitiator (Ciba), with 0.005 wt% methacryloxyethyl thiocarbamoyl rhodamine B (Polysciences) as a cross-linking fluorescent dye. The hydrophilic solution was composed of either 20 mol ethoxylated tri(methylol propane) triacrylate (20-ETMPTA, Sartomer) or poly(ethylene glycol) diacrylate (PEGDA, $M_n = 700$, Sigma Aldrich) at 80 vol%, 15 vol% deionized water,

and 5 vol% Darocur 1173 photoinitiator, with 0.005 wt% 3,8-dimethacryloyl ethidium bromide (Polysciences) as a cross-linking fluorescent dye.

3.3.3 Mask Design

Masks used for single-component fabrication contained two-dimensional arrays of identical aligned rods, with a separation in each direction equal to twice the length of the rod to avoid inter-particle curing. These arrays were designed to maximize the number of rods cured per cycle by making them large enough to, at minimum, cover the field stop aperture for the transmission of the UV beam. This circular aperture had a diameter of 1.5 inches. For example, the photomask containing 500 μm rod features was a twenty-by-twenty array, with the 1 mm separation ensuring that the mask area was large enough to use the full available UV beam. Masks used for Janus fabrication contained only a single line of rod features, with the rods parallel to one another and aligned perpendicular to the axis of the line. Spacing on these masks was the same as for single-component fabrication.

3.3.4 SFL Experiment

UV exposure and experimental imaging for small-rod fabrication was carried out using a 60x oil-immersion objective lens on an IX71 inverted microscope (Olympus America), with an additional 1.6x lens added to the beam path for the fabrication of smaller rods. Using the 60x objective, a demagnification factor of approximately 33 was typically observed between the mask and the resulting rods; i.e., a rod of 500 μm length defined on the photomask would typically result in the fabrication of a 12 μm rod in the microchannel.

Microchannel flow was driven by gas pressure supplied by a house nitrogen line and/or a compressed air tank (SJ Smith Welding Supply). Pressure control was

achieved using a custom-built pressure box consisting of four computer-controlled regulators and four duplex valves connected to a USB controller (National Instruments). This system allowed for up to four independent pressure settings driving up to eight separate valves. UV light was supplied by a 100 W mercury lamp connected in fluorescence microscope configuration with exposure time controlled using a Lambda SC electronic shutter (Sutter Instruments). The SFL experiment was driven using custom LabView software (National Instruments) using hardware drivers provided by the manufacturers. The process flow of an SFL experiment consists of the following sequence of steps:

1. Specify "flow time" t_{flow}, "pause time" t_{pause}, and "exposure time" t_{expose}.
2. Set pressure for each port on electronic regulators.
3. Until the experiment is stopped:
    (a) Open valves. Wait t_{flow}.
    (b) Close valves. Wait t_{pause}.
    (c) Open shutter. Wait t_{expose}.
    (d) Close shutter. Repeat.

For each monomer solution, a 10-100μL pipette tip (Eppendorf) was filled with approximately 60μL of solution. A silicone tube was connected at one end to the output of one valve of the pressure box, and the other end was inserted into the top of the pipette tip. The bottom of the pipette tip was then inserted into one of the small entrance holes in the microchannel device. This device was placed above the microscope objective, and the microscope was focused such that the focal place was inside the channel. After starting the experiment, the shutter was allowed to open and the fine focus was adjusted manually to optimize curing conditions. Optimization was judged by visual inspection of the resulting particles.

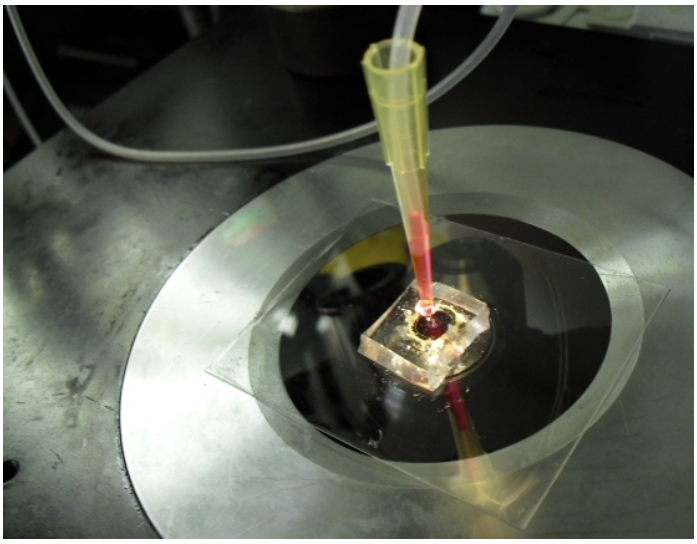

Figure 3.4: A microfluidic device platform containing multiple Y-junction microchannels is placed on the microscope used for SFL and connected to two pressure sources to pump PEGDA and TMPTA monomer solutions.

Single-component rods were fabricated using the central entrance channel to supply monomer to the system, leaving the other two entrances unused. (See Figure 3.4 for a photo of a single-component experiment.) Typical experimental settings for these experiments were pressure 8 psi, flow time 1.5 s, and pause time 2 s. This pause time was substantially longer than typical SFL pause times for larger particles, generally less than 0.5 s, due to the small height of the channels (see Equation 3.1). Exposure times for PEGDA or 20-ETMPTA were typically 0.05–0.15 s depending on the mask dimensions, while exposure times for TMPTA were typically 0.2–0.3 s to compensate for the less favorable curing behavior of the hydrophobic monomer. The fabrication of smaller rods generally necessitated slightly higher exposure times.

Janus rods were fabricated using the two side entrance channels to supply each type of monomer solution, with the central channel left unused (Figure 3.5). (All three channels were used for fabricating particles with complex anisotropy; see section 4.2.) Typical experimental settings for these experiments were pressure 7 psi on each side, flow time 2 s, pause time 2 s, and exposure time 0.2–0.3 s depending on the mask

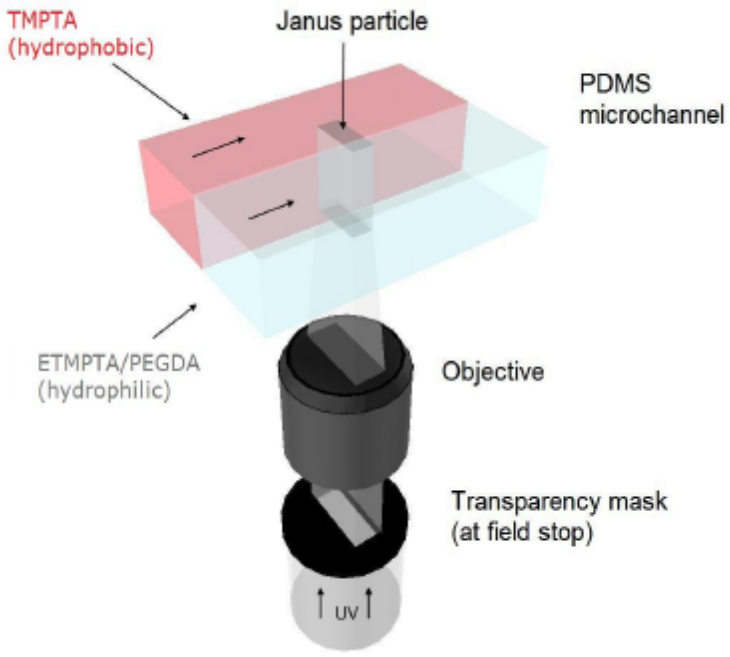

Figure 3.5: Janus rods are fabricated via SFL with two immiscible, co-flowing photocurable streams incorporating hydrophilic (PEGDA) and hydrophobic (TMPTA) monomer.

dimensions. The two monomer streams would enter the main channel on either side and form an interface along the center of the channel. Because the hydrophobic and hydrophilic streams were immiscible and the microchannel flow took place in the laminar flow regime, this interface persisted for several hundred microns down the channel. During fabrication, the curing regions would be aligned such that each rod straddled this interface, producing rods which incorporated both materials.

In either case, the resulting particles were ejected at the end of the experiment into the final reservoir, which was left empty to allow collection of the maximum volume of particles possible.

3.3.5 Particle Collection and Purification

Particle collection techniques were developed and optimized for a number of different experimental cases, depending both on the particular monomer solutions involved and on the desired final rod behavior, i.e., non-interacting or self-assembling. Details of the differences in collection techniques and their effectiveness will be explored in Section 3.4.1.

In general, SFL-fabricated rods were ejected, still in monomer solution, from the fabrication microchannel into an open reservoir, with the bottom and sides formed of PDMS and the top open to the laboratory environment. Owing to the surface tension of the monomer, these particles generally stayed near the side walls of the reservoir, often collecting in corners or imperfections of the walls. Note that in the single-component case, the particles in the reservoir may be assumed to be perfectly non-interacting as they are still suspended in the monomer solution, a solvent with the same composition as the particles. In the case of Janus rods this assumption is not necessarily valid, as the particles are suspended in a mixture of the two different monomer solutions. Once fabrication was complete, the collection procedure generally consisted of the following steps:

1. A collection solvent was introduced into the reservoir via the top opening, with volume sufficient to fill the reservoir (generally $\sim 20\mu L$).

2. A slight delay was allowed for the particles to disperse into the new solvent from their original position along the walls. This delay was not well-controlled, but was generally between 30 and 120 s.

3. A pipette was positioned in the reservoir with the tip near the highest concentration of particles, estimated manually using the microscope.

4. The pipette was used to collect a volume equivalent to the amount of collection

solvent introduced.

5. Repeat 3-5 times.

The particular solvent used, the dispersal time, and the type of pipette were all varied for different experimental cases; see Section 3.4.1 for details.

Following pipette collection, the particles were transferred either into a micro-centrifuge tube for solvent exchange or directly into an observation chamber. Solvent exchange was carried out in cases where the desired observation solvent was either incompatible with PDMS, such as toluene, or of sufficiently high viscosity to make direct collection difficult, such as in PEGDA. Solvent exchange was also used to reduce the concentration of the monomer solution components in the final solution, i.e., to remove liquid monomer and reduce the background fluorescence due to free dye.

To carry out solvent exchange, particles were placed in a micro-centrifuge tube and either centrifuged at 3000 rpm for 10 minutes or allowed to settle due to gravity for 6+ hours in order separate particles from solution. A quantity of supernatant solution equivalent to one-half the total volume was then carefully pipetted from the top of the tube, and replaced with the same quantity of the desired *observation solvent*. The tube was then agitated using a vortex mixer in order to mix the solvents and re-suspend the particles. This process was intended to be repeated seven times in order to increase the volume fraction of the new observation solvent to over 99%. However, experimental results indicating that this procedure resulted in heavy particle losses, with each additional exchange step reducing the yield significantly. Some experiments therefore included only a few exchange steps. The results of collection trials will be detailed in Section 3.4.1.

Observation chambers were constructed by affixing a glass coverslip to one end of short glass tube using five-minute epoxy (Devcon). Oriented with the coverslip

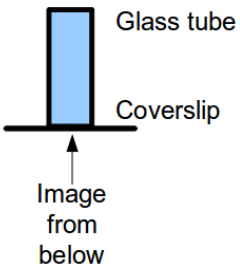

Figure 3.6: Design of a glass observation chamber for microscopy of particles.

as the base, this construct provides a flat transparent surface for microscopy. (See Figure 3.6.)

3.3.6 Diffusion Measurements

To carry out diffusion measurements, the rod sample was placed in the solvent of interest and pipetted into an observation chamber. In some cases the observation chamber was pre-coated with no-stick fluorosilane to inhibit sticking between the rods and the chamber surfaces; in others, the observation chamber was partially pre-filled with solvent in order to pre-wet the bottom surface, and the rods were allowed to settle for 20–30 minutes before observation.

The observation chamber was then placed on the sample stage of a fast confocal laser scanning microscope (CLSM; an IX71 inverted microscope, Olympus America, connected to a vt^{eye} confocal scanner, Visitech International). The CLSM included two independent excitation laser lines with peak wavelengths of 491 nm and 561 nm, corresponding to our ethidium bromide and Rhodamine B dyes. A 100x oil-immersion objective lens was used for imaging the rods which had settled at the bottom of the chamber. The microscope was initially used in bright-field imaging mode and manually adjusted to visually find the particles and optimize the focus.

Following the bright-field adjustments, the microscope was put into confocal mode, the laser line selected based on the particular sample, and two-dimensional rod diffu-

sion at the bottom of the chamber was imaged in time-series mode. The microscope was configured such that images were acquired at a rate of 1 frame per second (fps), each image consisting of the average of eight frames acquired at 30 fps. After this acquisition (8/30 s long), the laser shutter is closed until the next one-second image is aquired to minimize photobleaching. (For fast diffusion of the smallest rods, image acquisition was adjusted to 2 fps.) Laser exposure was triggered only during active acquisition, and shuttered otherwise. Image dimensions were 512 $\times$ 512 pixels with a scale of 10 pixels per μm, and each pixel's intensity was scaled over eight bits to assume values in the range of 0–255. The intensity scale was adjusted relative to the actual intensity to maximize the dynamic range for the particular sample. The total time of a typical experiment was 10 minutes.

Time-series image data were saved as 8-bit TIFF image stacks and transferred to computation servers for analysis. Analyses were carried out to compute mean-square-displacement and orientation displacement for each rod using the algorithms as described in Section 2.3 and implemented in Matlab scripts described in Appendix A. These data were used to calculate two-dimensional diffusion constants.

3.3.7 Large-Area Imaging

Large-area imaging experiments were carried out using the Zeiss Axiovert 200M inverted fluorescence microscope in the Imaging Technology Group at the Beckman Institute. Sample observation chambers with radii between 0.7 and 2 mm were used. Samples were imaged using the 60x objective lens. Large-area images were obtained by taking tiled images of dimensions up to 9 $\times$9 images, covering total areas of up to 2 mm^2. These images were then stitched together with overlap areas of 10% using Axiovision software, and new color balance and background images obtained before each new acquisition experiment.

3.4 Results and Discussion

3.4.1 Collection Techniques

In principle, collection of colloidal rods after SFL fabrication should be relatively simple, given that the procedure outlined in Section 3.3.5 for the collection of rods seems intuitive and straightforward. However, initial collection and processing experiments with small colloidal rods resulted in extremely low yields, with additional losses in each subsequent processing step.

Collection Solvents

Solvent	PEGDA	TMPTA	Janus
Organic solvents			
Ethanol	Yes	Yes	Yes
IPA	Yes	Poorly	Poorly
Toluene	Poorly	Yes	Poorly
Monomeric solvents			
PEGDA	No	No	No
ETMPTA	No	No	No
TMPTA	No	No	No
Ethylene glycol	Poorly	No	Poorly
Polar solvents			
Water	Yes	No	Poorly
DMSO	Yes	Yes	Yes

Table 3.1: PEGDA, TMPTA and Janus rods may be collected using different solvents. "Yes" indicates that a single pipette collection can successfully extract more than 80% of the particles; "Poorly" indicates that a single collection extracts more than 50% of the particles but less than 80%; and "No" indicates that a single collection extracts fewer than 50% of the particles.

Several different collection solvents were explored for experiments involving both Janus rods and single-component hydrophilic and hydrophobic rods. The solvents used included common organic solvents such as ethanol, isopropyl alcohol (IPA), and toluene; solvents with similar chemistries to the particles, including solutions of

PEGDA, ETMPTA, TMPTA, and ethylene glycol; and the common polar solvents water and dimethyl sulfoxide (DMSO). Collection solvents were compared to each other based on estimating the fraction of particles which remained in the fabrication reservoir following the first pipette step. Collection was deemed successful (a "yes" in the table) if fewer than 20% of particles remained; "poorly" represents fewer than 50% remaining; and failure (a "no" in the table) if more than 50% of the particles remained after pipetting. The results of these trials are presented qualitatively in Table 3.1. To summarize, the best results were generally found with the organic solvents, with ethanol being a good all-purpose collection solvent. Collection with solvents similar to the monomer were generally unsuccessful, with repeated pipetting failing to remove more than 20-30% of particles. Water was useful only in the collection of PEGDA rods. DMSO was also fairly successful, but demonstrated more of a tendency to swell the PDMS and was more hazardous to work with than ethanol.

Pipettes and Micro-Centrifuge Tubes

While removing particles from the reservoir was successful for some solvents, the second part of the collection procedure, demonstrated ejecting those particles from the pipette into a second container, was much less successful. Simple trials in which particles were extracted from the fabrication reservoir and then deposited directly into observation chambers using standard plastic pipette tips showed yields of less than 50%, even when 90% or more of the particles had been shown to leave the reservoir.

Several different types of pipettes were used, including 15 μL plastic pipette tips (Eppendorf), glass pasteur pipettes, and glass microcapillaries extracted using micropipette bulbs. Each of these was also coated with fluorosilane to attempt to reduce adhesion between the particles and the pipette surfaces. The use of either type of glass pipette typically increased yield to close to 60%. Fluorosilane coatings on the

glass pipettes showed additional improvements to 65-70%, but this improvement was unreliable. Yield of the fluorosilane-coated plastic tips was decreased relative to the uncoated tips.

In addition, yield was also substantially reduced when particles were transferred to a microcentrifuge tube and then re-extracted, with yields of less than 10% of the particles placed in the tube. This yield was not improved by fluorosilane vapor-coating or by the use of any other solvent and had significant negative effects on solvent exchange and particle cleaning procedures. In many experiments, cleaning steps were neglected entirely to preserve sample volume, with possible negative effects on the final results.

3.4.2 Surface Interactions

Ideally, all experiments involving SFL particles should take place in an experimental chamber in which all non-particle surfaces are repulsive with respect to all particle chemistries, so that particles may diffuse and interact without being affected by extraneous surface forces. Unfortunately, this is a difficult demand to satisfy, especially in the case of Janus rods which incorporate both hydrophilic and hydrophoic functionalities.

In order to better understand this constraint and optimize future experiments, several different chamber surface functionalities were selected: a hydrophobic PDMS surface, a hydrophilic pirahna-rinsed glass surface, and both PDMS and glass surfaces that had been vapor-coated with the same fluorosilane material used to coat photoresist masters, chosen to potentially minimize sticking with either particle functionality. Particle-surface interactions were measured qualitatively by suspending 6 μm single-component rods of either hydrophobic or hydrophilic functionality in a series of different solvents. The observation chamber surface functionality was also varied. The diffusion of these rods was then observed via CLSM to determine whether or not they

were free to diffuse in that particle/surface/solvent combination. The results of these experiments are summarized in Table 3.2.

Particles free to move?					
Solvent	Material	Glass	PDMS	Glass-Silane	PDMS-Silane
Water	PEGDA	No	Hindered	No	No
	TMPTA	No	No	No	No
Ethanol	PEGDA	No	No	No	Yes
	TMPTA	No	No	No	No
DMSO	PEGDA	No	No	No	No
	TMPTA	No	No	No	No
IPA	PEGDA	No	No	No	No
	TMPTA	No	No	No	Hindered
Toluene	PEGDA	No	Hindered	No	No
	TMPTA	Yes	Yes	No	Hindered

Table 3.2: Freedom of diffusion on different surfaces is characterized as either "yes" (free to move), "no" (stuck to the surface), or "hindered" (moves only when externally agitated).

Unfortunately, in the majority of cases the particles were found to be firmly stuck to the internal surfaces of the observation chamber, with only a few particle/surface/-solvent combinations allowing free particle movement even under external agitation. No combination allowed particles of both materials to move freely without agitation at the same time. The most successful combination, suspension in toluene on PDMS surfaces, allowed free motion of TMPTA particles and motion only under agitation for PEGDA particles. The flurosilane-coated surfaces showed no particular improvement over either bare PDMS or glass.

This lack of free motion may be at least partially caused by the presence of residual unreacted monomer mixed into the solvent, which may stick to the particle surfaces and enhance adhesion between the particles and the chamber surfaces. This monomer is still present due to the difficulties in collecting and cleaning the particles outlined in Section 3.4.1.

3.4.3 Translational and Rotational Diffusion

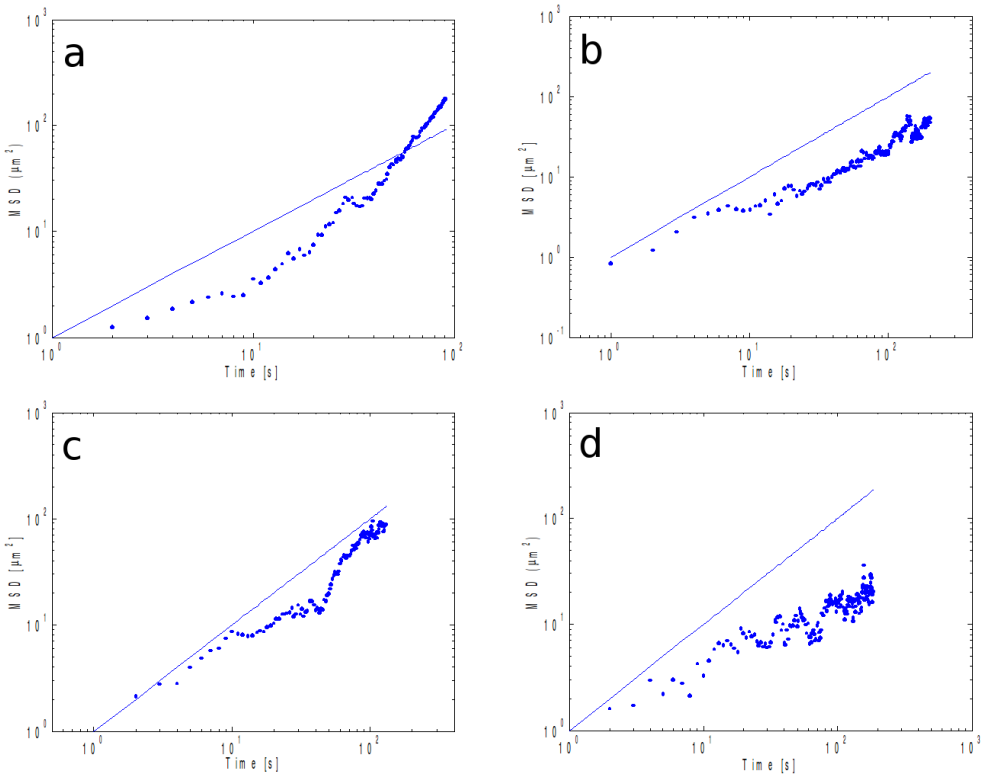

Figure 3.7: MSD plots for (a) 6 μm rods, (b) 9 μm rods, (c) 12 μm rods, and (d) 15 μm rods. The straight lines have a slope of one, representing ideal diffusion behavior.

Dynamics experiments were carried out to study the effect of rod size and aspect ratio on the rate of diffusion. To ensure that we study only the effect of changing rod dimensions, the results of Section 3.4.2 were used to select a system with maximized rod mobility. Single-component TMPTA rods with lengths of 6, 9, 12, and 15 μm were suspended in toluene and transferred to glass-bottom confocal observation chambers. These chambers had also been pre-rinsed in toluene. The rod samples were then observed by CLSM under the conditions described in Section 3.3.6 for time-series experiments. The resulting 2D image series were processed and analyzed using the algorithm described in Section 2.3, and the translational and rotational mean-square displacements (MSD) were calculated and plotted. The translational MSD are plotted

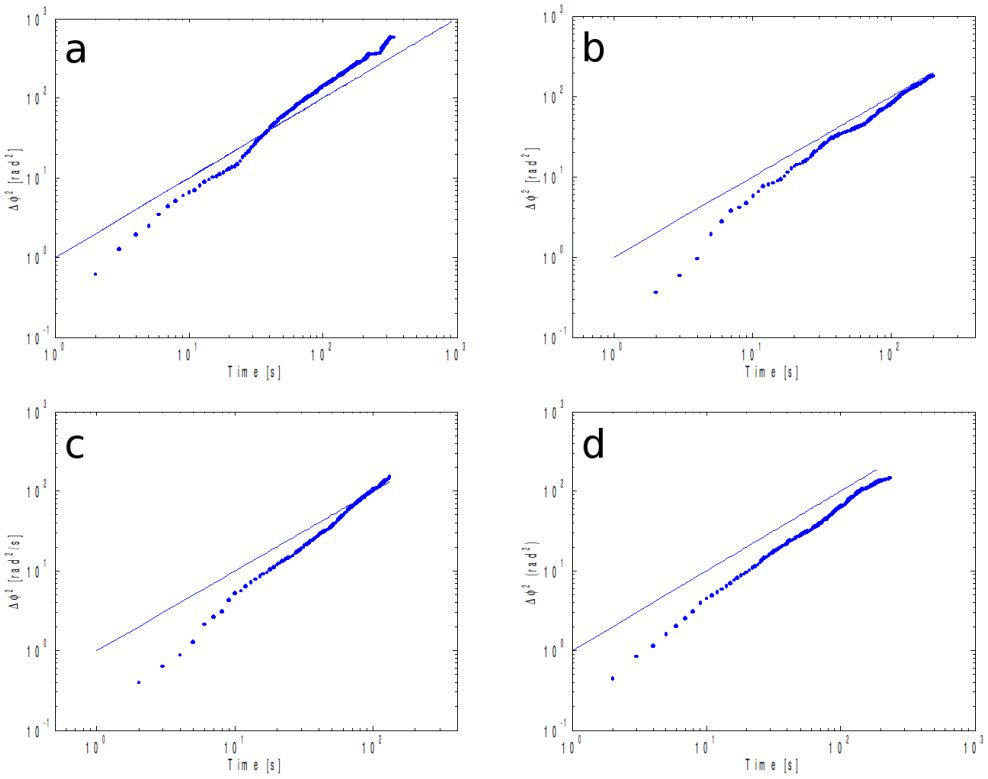

Figure 3.8: Rotational MSD data plots for (a) $6\mu m$ rods, (b) 9 μm rods, (c) 12 μm rods, and (d) 15 μm rods. The straight lines have a slope of one, representing ideal diffusion behavior.

with respect to time in Figure 3.7, and the rotational MSD are plotted with respect to time in Figure 3.8.

Translational and rotational MSD may be related to the translational and rotational diffusion coefficients, D and θ, according to Equations 3.2 and 3.3, respectively. Experimental values for these constants were calculated for each of the four rod lengths by performing least-squares regression linear fits to determine the slope of plots of MSD vs. time. The resulting diffusion coefficients are shown in Table 3.3 and are compared to theoretical values calculated from Equations 3.4 and 3.5. [5] It is interesting to note that in all cases, the experimental diffusion coefficients are measured to be larger than the theoretical values. This may be attributable to the fact that we are observing 2D diffusion near a surface rather than 3D diffusion, which could affect

the calculation of either or both of the experimental and theoretical values.

Rod length [μm]	$D_{exp}(D_{th})$ [$\mu m^2/s$]	$\theta_{exp}(\theta_{th})$ [rad^2/s]
6	0.77 (0.19)	1.21 (0.81)
9	0.22 (0.12)	0.80 (0.24)
12	0.29 (0.093)	0.76 (0.10)
15	0.17 (0.074)	0.59 (0.052)

Table 3.3: Translational and rotational rod diffusion coefficients are calculated for the experimental data through fitting of MSD data. The theoretical diffusion constants are also calculated (coefficients in parentheses). [5]

$$< [r(t) - r(0)]^2 >= 4Dt \tag{3.2}$$

$$< [\phi(t) - \phi(0)]^2 >= 4\theta t \tag{3.3}$$

$$D = kT/3\pi\eta_s L \tag{3.4}$$

$$\theta = (3kT/\pi\eta_s L^3) \log 2L/d \tag{3.5}$$

3.4.4 Self-Assembly of Janus Rods

Initialy, Janus fabrication was carried out using microchannels fabricated with a height of 15 μm, producing relatively large Janus rods (Figure 3.9) with dimensions

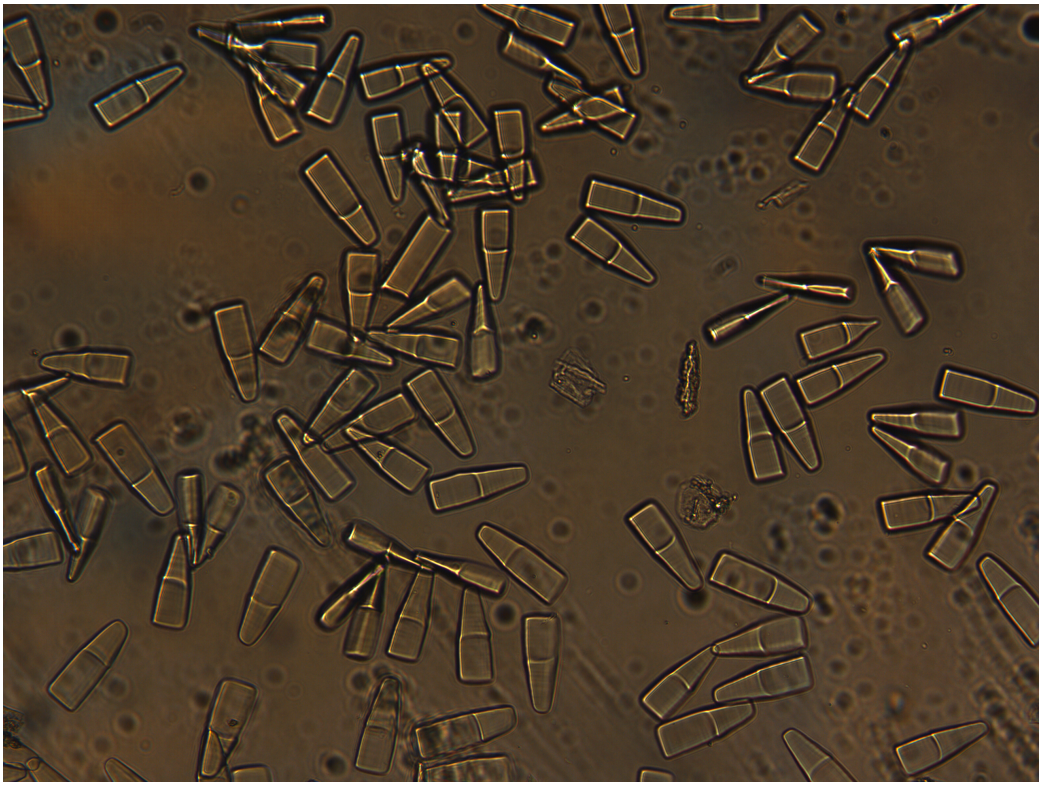

Figure 3.9: Large Janus rods (45 x 11 x 11 μm), randomly oriented. The narrower ends are composed of hydrophobic TMPTA, while the broader ends are composed of hydrophilic PEGDA. The narrowing of the TMPTA ends was caused by a contraction due to an error in the monomer concentration for these experiments.

of roughly 45 $\times$11 $\times$11 μm. In these experiments only, the hydrophobic material is un-dyed while the hydrophilic material is dyed using Rhodamine B. These rods exhibited little spontaneous self-assembly in water, but agitation of these particles drove their rearrangement into new self-assembled configurations, producing clustered structures with high contact areas between the hydrophobic regions of the particles (Figure 3.10). This experiment serves as a proof-of-concept of hydrophobic self-assembly and a duplication of the results from the amphiphilic particle experiments in Dendukuri *et al.* [31]

Next, the fabrication microchannel was reduced in height to 7 μm and the mask size was varied to explore the size limitations in fabricating Janus rods. Janus rods

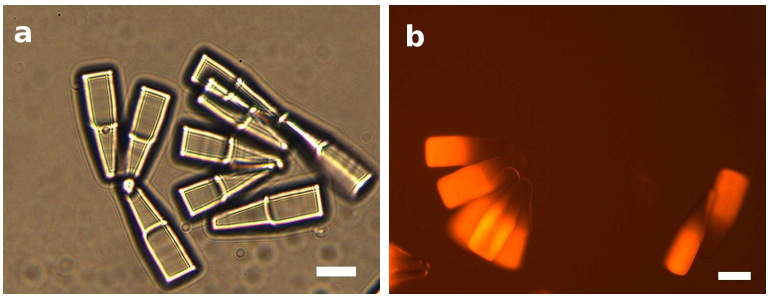

Figure 3.10: Large Janus rods self-assemble following agitation. The hydrophilic ends are dyed with Rhodamine B.

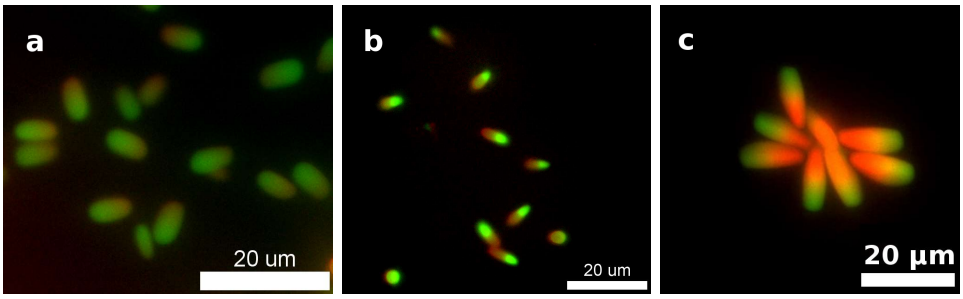

Figure 3.11: Janus rods with lengths of (a) 4 μm, (b) 7 microns, and (c) 15 microns may be produced by changing the mask dimensions.

were successfully fabricated using 200 μm, 300 μm and 500 μm masks to produce Janus rods with lengths of 4 μm, 7 μm and 15 μm respectively. Particle width in all cases was $\simeq$ 3 μm, defined by the photomask, the microchannel height and the thickness of the oxygen inhibition layer. (See Figure 3.11(a,b,c).)

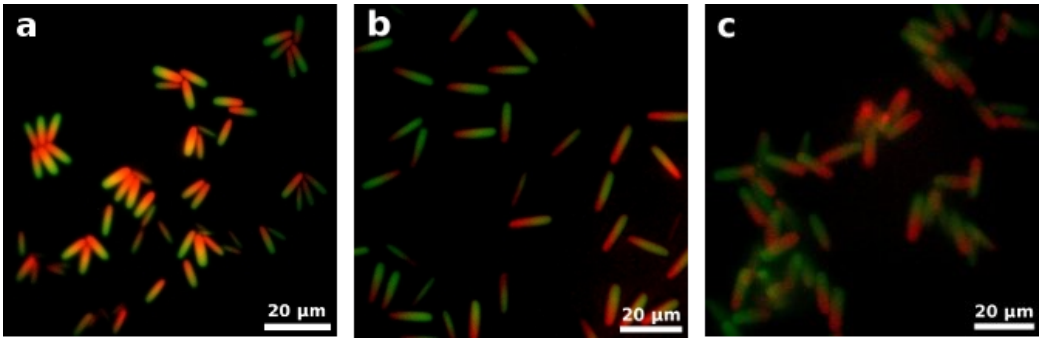

Figure 3.12: Self-assembly of Janus rods in (a) water, (b) DMSO and (c) IPA.

To explore the effect of the solvent conditions on the self-assembly behavior, identical Janus rod samples with rod dimensions of 12 $\times$3 $\times$3 μm were fabricated and placed in three different solvents: water, dimethyl sulfoxide (DMSO) and isopropyl alcohol (IPA). In water, we saw a result similar to that seen for the large Janus rods, with strong hydrophobic self-assembly producing structured clusters with strongly-correlated orientations between the rods within a cluster. Suspension and agitation in DMSO, however, showed no appreciable self-assembly. This result is consistent with the lower polarity of DMSO, decreasing the driving force for hydrophobic self-assembly. Moving the particles to IPA, a non-polar solvent, showed a completely different self-assembly behavior following agitation, in which the green-dyed hydrophilic ends of the particles assembled to maximize contact area. This series of experiments illustrated the potential for control of self-assembly through variation of the solvent conditions.

Focusing on self-assembly in water, we see that a variety of different structures may be achieved. In a single sample, local variations in concentration due to uneven

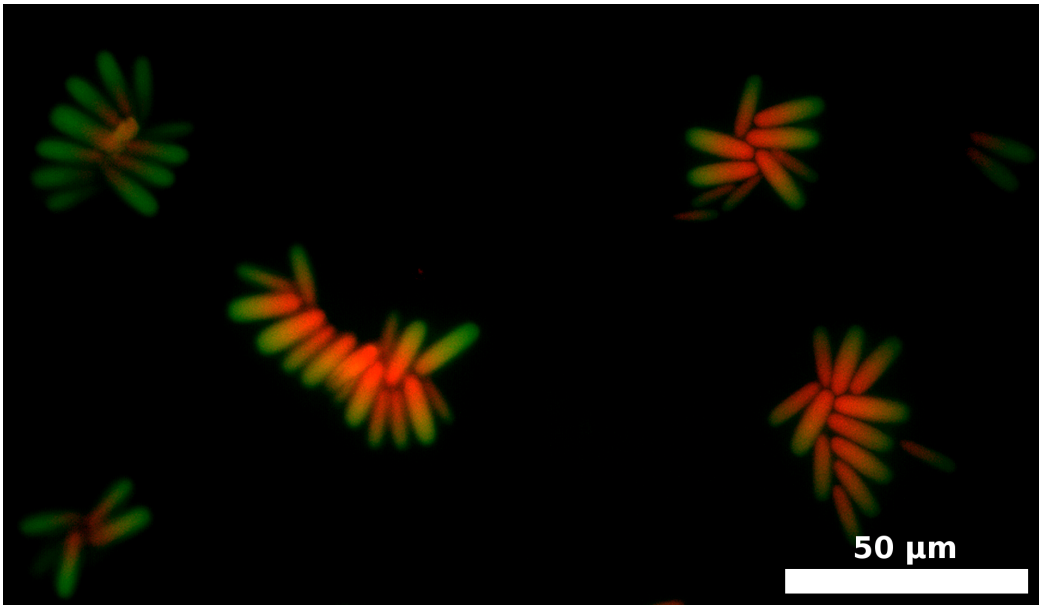

Figure 3.13: Janus rods self-assemble at low concentrations into small "micellar" clusters.

mixing may produce dramatically different results. Where the local concentration is low, highly-ordered clusters are produced which have a "micelle-like" geometry with the particles grouped around a common center where the hydrophobic regions tend to maximize contact area (Figure 3.13). Where the local concentration is high, however, extended structures containing many more particles may be formed (Figure 3.14). These structures have a "gel-like" motif in that they are more randomly arranged but still contain sub-clusters which are formed by hydrophobic assembly.

A more quantitative study of Janus rod self-assembly was attempted by fabricating large numbers of Janus rods and observing their self-assembly in confocal observation chambers. Fabrication sample size for each experiment was approximately 50,000 particles; losses due to transfer and processing reduced this to an estimated 20,000 particles. Two parameters were varied: the assembly solvent, which was a mixture of DMSO and water with the relative fraction adjusted; and the aspect ratio of the particle, which was varied in the range of 1.5-4.5. Large-area images were acquired as

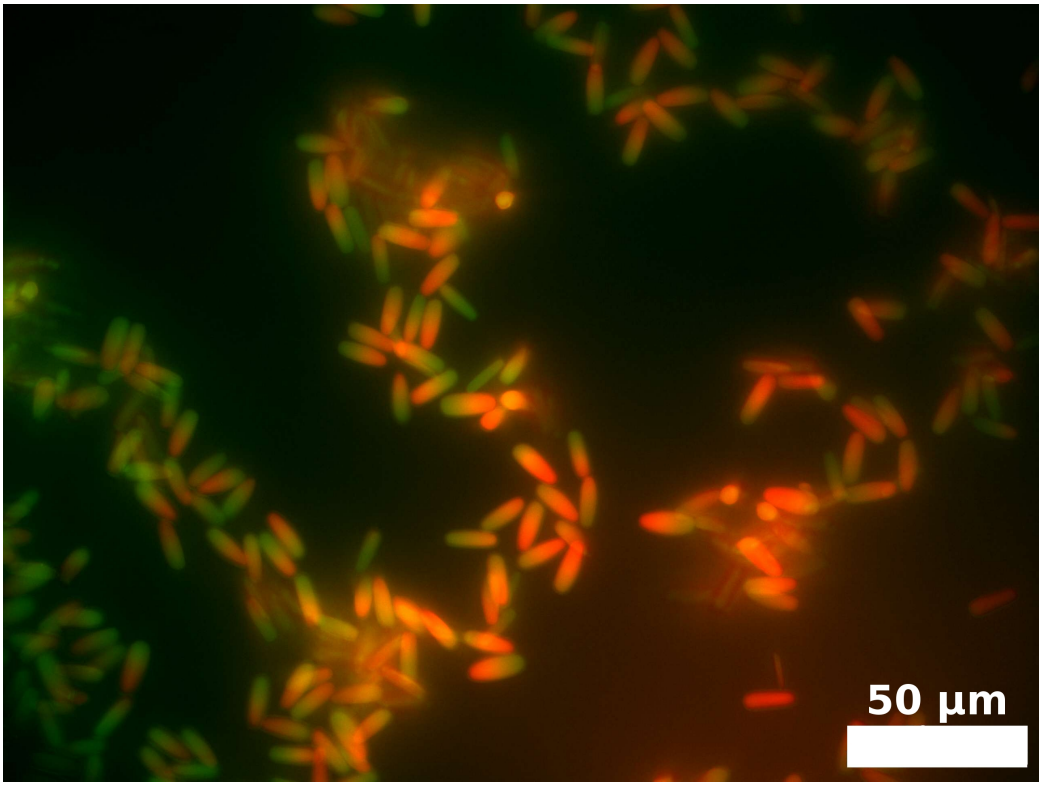

Figure 3.14: Janus rods self-assemble at high concentration into extended, gel-like structures in water.

detailed in Section 3.3.7 and analyzed as detailed in Sections 2.3 and A.7.2. Sample images at low and high magnification are shown in Figure 3.15.

Two parameters were calculated for each sample: the average number of contacts or "bonds" per particle, and the degree of orientational ordering for particles in the same cluster. The number of "bonds" was calculated as the number of particles which were found within a center-to-center distance equal to one rod length. The orientational ordering was measured as the average dot product of the orientation vectors between pairs of rods which were considered to be in the same cluster, with clusters defined according to the same bond criterion. The results of these calculations are plotted for all experiments in Figures 3.16 and 3.17. Unfortunately these results are somewhat contradictory, and it is difficult to draw strong conclusions about the behavior of Janus rods undergoing self-assembly. However, it is possible to make a

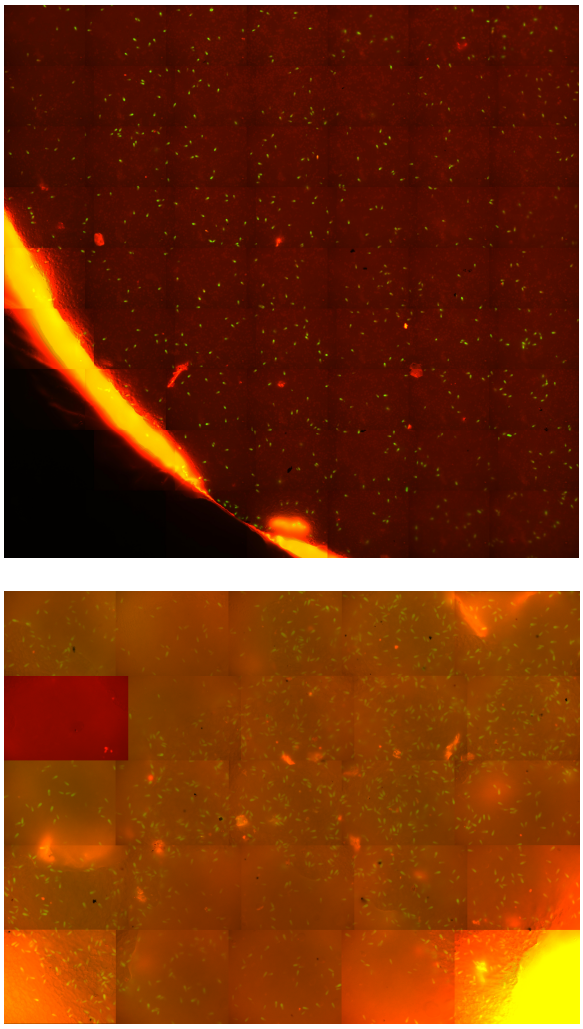

Figure 3.15: Two large-area views of Janus rod self-assembly in DMSO/water, the bottom view at a higher magnification. Both images were produced by tiling multiple fluorescence microscopy images taken at different positions in the sample (see Section 3.3.7).

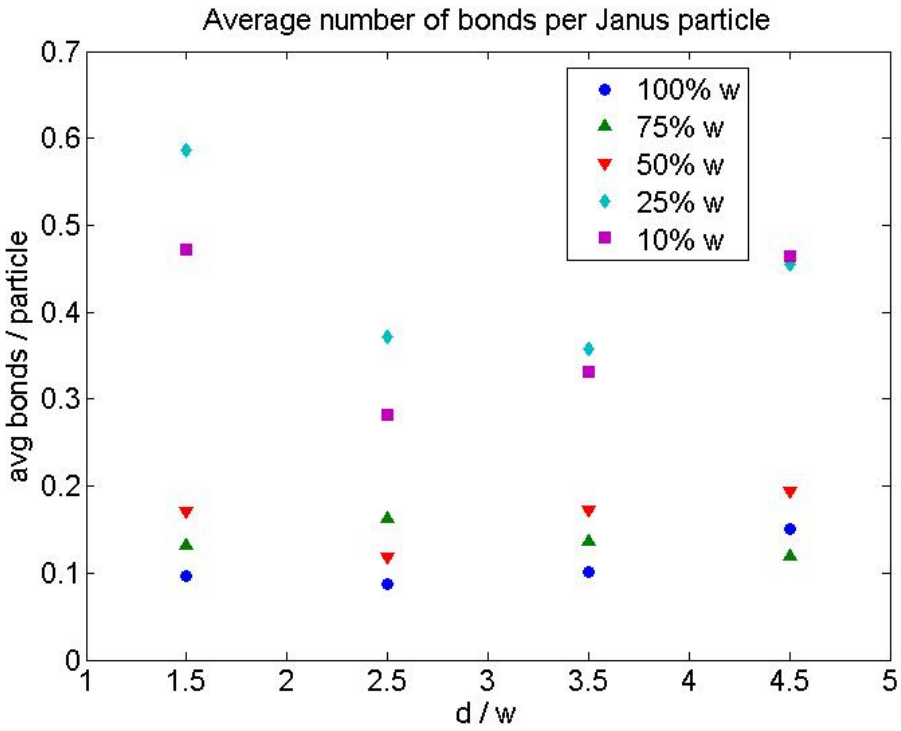

Figure 3.16: The average number of nearest neighbors of "bonds" per Janus particle is determined for samples of different aspect ratios (d/w) and solvent composition. Solvents are DMSO/water mixtures, with composition measured according to the water fraction (% w).

few general comments.

The first thing that should be noted is that for all experiments, the average number of bonds per particle never exceeds about 0.6, and in fact most experiments have bond numbers below 0.2. This can be attributed to the fact that despite the high number of particles fabricated relative to typical SFL experiments, the rod concentrations are still quite low: settled to the bottom of the container, the average areal concentration never exceeds about 5%. The bond numbers for DMSO/water mixtures of 50–100% water are all relatively similar, in the range of 0.1–0.2, and do not vary dramatically with aspect ratio.

For solutions with greater than 50% DMSO, however, we see a striking increase in bond number. Without carrying out additional experiments it is difficult to determine

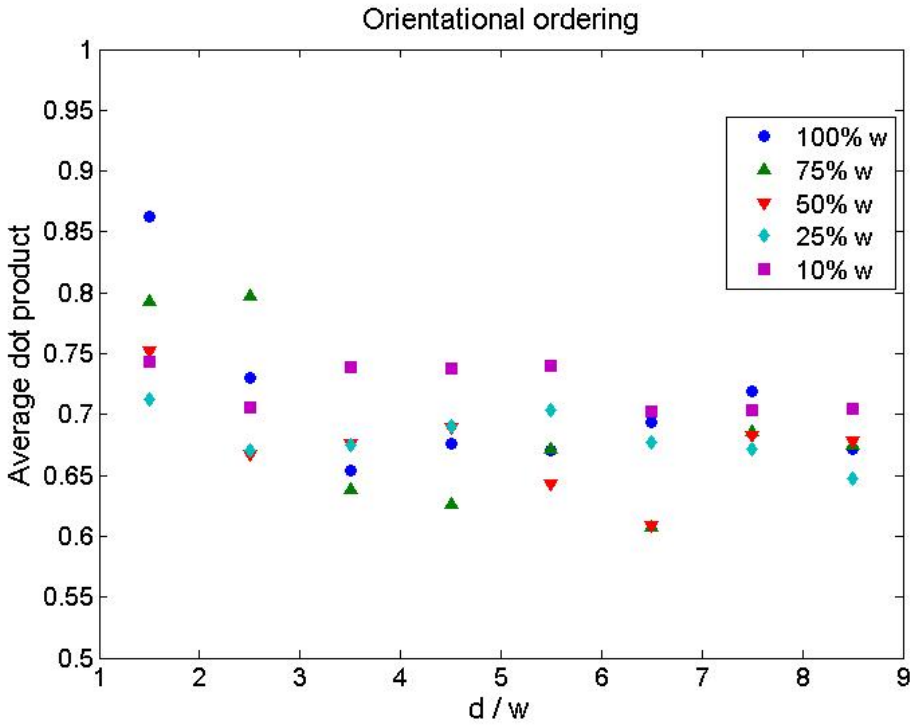

Figure 3.17: The orientational ordering of Janus rods within a cluster, as represented by the mean dot product of orientation vectors in rods within the same cluster, is determined for samples of different aspect ratios (d/w) and solvent composition. Solvents are DMSO/water mixtures, with composition measured according to the water fraction (% w).

the cause of this increase. We might speculate that the higher density of DMSO and the consequent slower settling might allow the rods more time to "find" one another and assemble, but in this case we would expect a more continuous variation of bond number with DMSO concentration. Another cause might be an experimental anomaly which increased the final particle yield in the high-DMSO samples relative to the others. Within these samples, however, we see a consistent variation in bond number with respect to aspect ratio, with much higher bond numbers observed at low and high aspect ratios. The increase in bond number at low aspect ratio, and thus low particle size, might be attributed to the higher mobility of these particles on a surface where Janus particles would tend to stick (see Section 3.4.2), while the increase at

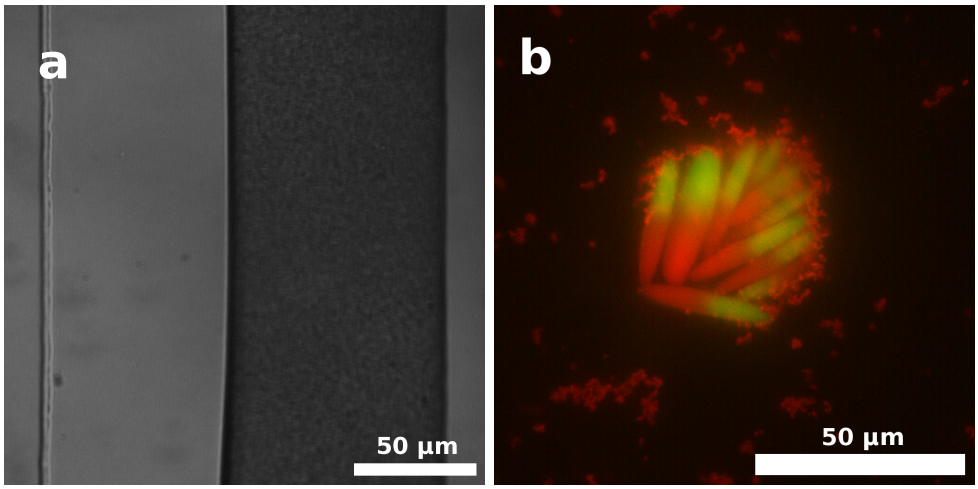

Figure 3.18: (a) Ag nanoparticles are suspended in PEGDA monomer solution at a concentration of 5 wt% for Janus SFL fabrication. The resulting Janus rods (b) contain embedded Ag nanoparticles.

high aspect ratio may be due to the higher opportunity for contact available with longer rods.

Turning our attention to the orientational ordering, we see much more consistent results across the range of solvent compositions, with little in the way of consistent discernible variation between samples with the same aspect ratio. A dot product of 1.0 implies perfect parallel ordering, while a dot product of 0.0 implies perpendicular ordering; average values close to 0.5 may be interpreted as showing relatively random orientation within the sample. With that in mind, it is interesting to note that particles with low aspect ratio show a relatively strong ordering, and that the dot product decreases towards randomness as the aspect ratio increases. This is somewhat counter-intuitive and contradicts previous imaging which would suggest better correlation between particles with a high aspect ratio.

3.4.5 Potential Applications

The potential for the incorporation of functional materials into SFL Janus particles was explored in a pilot experiment involving the incorporation of Ag nanoparticles (NPs) into the hydrophilic PEGDA monomer solution at 5 wt%. A Janus fabrication experiment using this solution was performed, and the Ag NPs were shown not to interfere with the establishment of a stable pair of co-flowing streams (see Figure 3.18(a)). Standard Janus SFL was carried out using a 400 μm mask to produce 12 μm Janus rods. When placed in water, these rods self-assembled normally, as shown in Figure 3.18(b). Note, however, the presence of free Ag NPs (fluorescing red) both in free solution and aggregated around the assembled cluster. This illustrates that the successful rinsing and removal of functional materials from the suspension solvent remains a major difficulty in incorporating any functional material in SFL.

Chapter 4

Fabrication and Self-Assembly of Exotic Colloids

4.1 Introduction

Stop-flow lithography (SFL) has been demonstrated to be useful for fabricating particles with simple geometric and chemical anisotropies, such as a high aspect ratio and two-sided Janus functionality. With this shown, the next question becomes, can the same technique be used to produce other forms of anisotropy? In this chapter, the fabrication of particles with branched anisotropy is explored, and the hydrophobic self-assembly of these particles is demonstrated in polar solvent. More exotic functionalities are also explored, including particles whose assembly may take different forms depending on the driving force.

4.2 Experimental Procedure

4.2.1 Three-Stream Experiment

SFL experiments were carried out using the device design described in Section 3.3.4 (see Figure 3.3). All three input channels were used for the fabrication of branched and other exotic particles, with the typical monomer inputs being PEGDA solution in the center channel and TMPTA solution on the left- and right-hand inputs. (See Section 3.3.2 for a full description of these solutions.) Typical initial pressures for microchannel flow were 8 *psi* for the left- and right-hand inputs and 6 *psi* for the

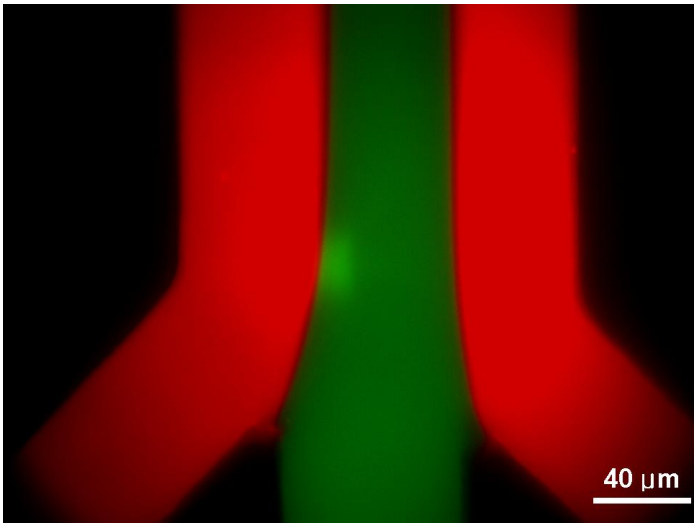

Figure 4.1: Fluorescence image of a microchannel during three-stream flow.

center input. Typical values for t_{flow}, t_{pause} and t_{expose} were 2.0 s, 2.0 s and 0.25 s, respectively. SFL fabrication masks were designed for three-stream fabrication in a manner similar to the masks used for the fabrication of Janus rods, with several identical particle patterns arranged in a single line. These masks could then be aligned to allow polymerization overlapping the two parallel TMPTA/PEGDA interfaces.

All SFL parameters were adjusted at the beginning of each experiment to optimize fabrication conditions. A number of constraints were applied in order to achieve consistent results for the fabrication of multiple-component particles, including:

- t_{flow} sufficient to eject particles following polymerization.
- t_{pause} sufficient for a complete stop in flow, to optimize polymerization conditions.
- t_{pause} small enough to prevent the center stream from breaking up into droplets.
- t_{expose} sufficient to fully cure particles.
- Relative pressures optimized to produce a jetting flow with a sufficiently narrow stream for fabricating small particles.

The major difficulty in this experiment was balancing the relative pressures and flow times to produce PEGDA/TMPTA interfaces which were sufficiently narrow for the fabrication of the particles of interest while still avoiding the break-up of the center stream into a series of droplets ("dripping mode"). This set of constraints imposed strict limits on the minimum size of the particles, with the minimum width achieved for the center stream being approximately 12 μm. Due to the presence of air bubbles and imperfections in the microchannel, this optimization had to be performed for every experiment and greatly reduced consistency between subsequent fabrication experiments.

4.2.2 Collection and Processing

Complex Janus particles were ejected from the fabrication channel while still in monomer solution and collected in an open reservoir. The particle collection procedure was identical to that outlined in Section 3.3.5. Ethanol was used as the collection solvent, and glass Pasteur pipettes were used to extract the particles. All particles samples were washed by microcentrifuge solvent exchange using ethanol, and were transferred to glass observation chambers in either ethanol (for simple fluorescence observation) or in water (for observation of self-assembly).

4.3 Results and Discussion

4.3.1 Branched Particles

Figure 4.2: Anisotropy dimension: branching. [1]

SFL fabrication experiments were performed with masks designed to target the branching morphologies portrayed in the scheme of anisotropy dimensions outlined by Glotzer and Solomon (see Figure 4.2). [1] As single-component rods and two-part Janus rods had been accomplished in Chapter 3, the following particle morphologies were targeted: hydrophilic rods with hydrophobic patches on either end, three-branch particles with hydrophobic ends, and four-branch particles with hydrophobic ends.

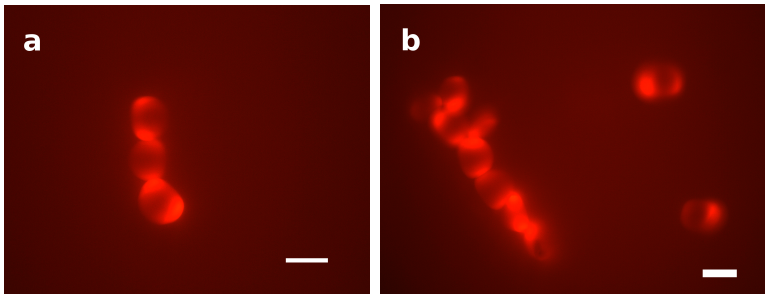

Figure 4.3: Chain-like assembly of tall two-patch particles. Scale-bar is 20 μm.

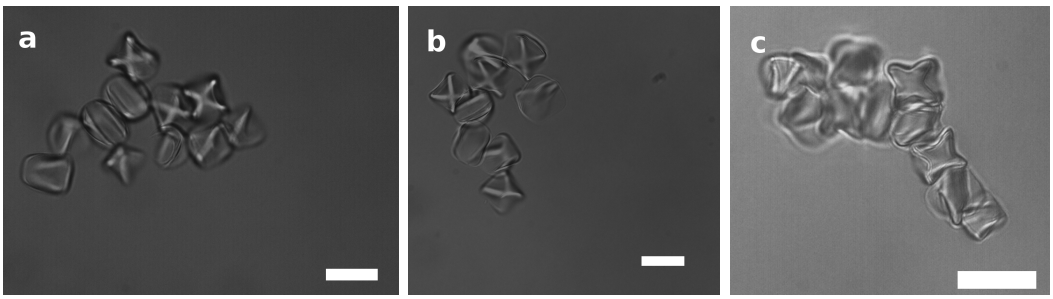

Figure 4.4: Self-assembly of tall four-patch particles. Scale-bar is 20 μm.

As with Janus rods, initial experiments were carried out in "tall" microchannel devices with a height of 15 μm to produce larger particles which might be more easily studied. These proof-of concept experiments were carried out to produce two-patch and four-patch particles with heights of roughly 11 μm and width of 20 μm.

These particles were then transferred into water suspension to study self-assembly. Two-patch particles were observed to form linear chain-like structures with end-to-end assembly, as seen in Figure 4.3. This is dramatically different from the micelle-like

clusters formed by Janus rods, shown previously in Figure 3.13. Four-patch particles assembled into denser clusters due to their additional assembly sites, producing structures which combined chain-like morphologies (Figure 4.4(c)) with dense and loop-like structures (Figure 4.4(a,b)).

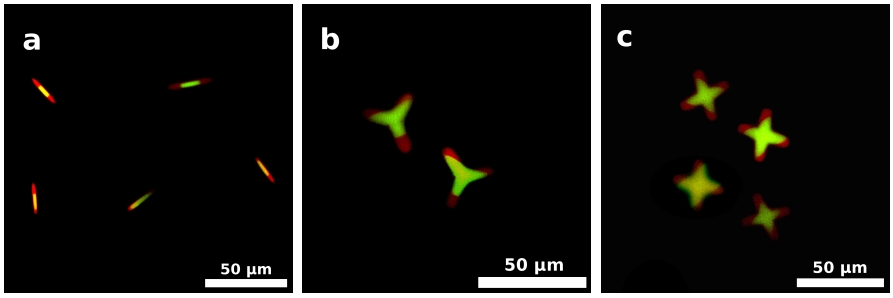

Figure 4.5: Two-component particles with (a) two, (b) three and (c) four hydrophobic patches.

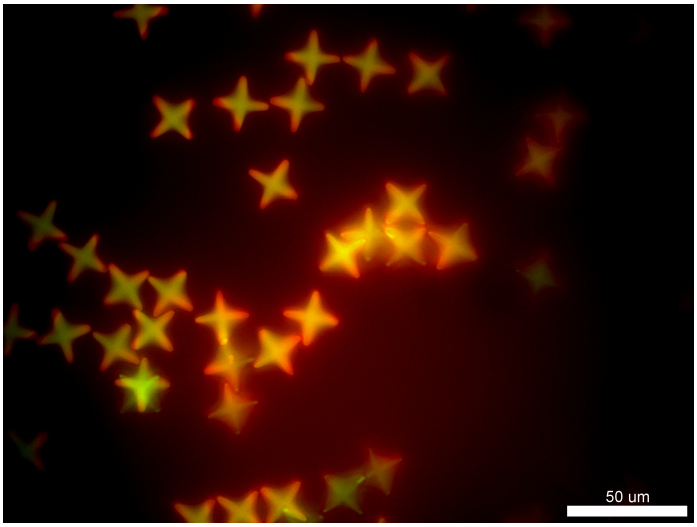

Figure 4.6: Janus crosses are suspended at high concentration and self-assemble by contact of hydrophobic "patches" at the end of each arm..

Following this demonstration, subsequent experiments focused on producing high-quality branched Janus particles using microchannels with a height of 7 μm. These experiments were carried out to produce representative examples of particles with two, three and four patches with heights of 3 μm and lateral dimensions of approximately

30 μm.

Unfortunately, due to the considerations outlined in Section 4.2, these experiments failed quickly and rarely produced more than a few particles at a time. One relatively large sample of a 3000 four-patch "crosses" was successfully fabricated and suspended in water to observe their self-assembly; a fluorescence microscopy image of this sample is shown in Figure 4.6. Here we can see some strongly-aligned self-assembly, with crosses generally arranging themselves such that their hydrophobic ends are maximizing contact area. This is a flexible mode of self-assembly, which may enable the formation of many different superstructures, and this image alone shows several different cluster morphologies.

4.3.2 Multiple Modes of Assembly

Figure 4.7: Two possible modes of self-assembly for Janus "boomerangs": (a) geometric, and (b) open and hydrophobic

In addition to the branched particles illustrated above, we attempted to design and fabricate a particle which might undergo two or more different types of self-assembly depending on the environment in which it was placed.

To achieve this, we designed a "boomerang" particle incorporating hydrophobic ends. Under neutral solvent conditions, such as a weakly-polar solvent such as DMSO, these particles might be induced to undergo a dense geometric self-assembly with cluster morphology dictated by the particle shape. An example of such a structure is illustrated in Figure 4.7(a). Such an assembly might be induced by the introduction

of a low-molecular-weight polymer to induce a depletion interaction. To achieve the second assembly mode, the particles would be placed in a strongly-polar solvent such as water in order to drive a hydrophobic attraction between the particle ends, thus producing a more randomly-oriented and open structure such as the one illustrated in Figure 4.7(b).

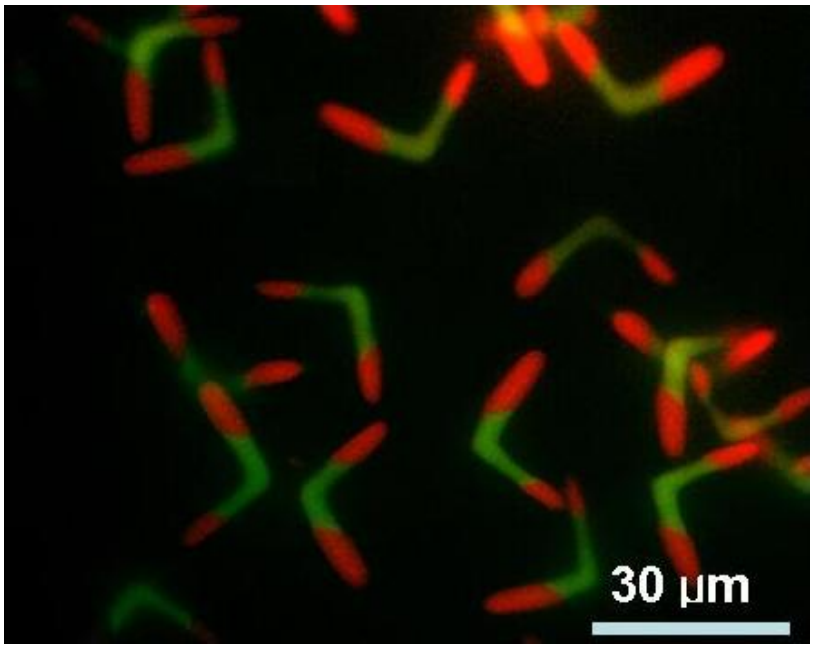

Figure 4.8: Fluorescence image of Janus "boomerangs" suspended in DMSO.

Large boomerang-type particles were successfully fabricated by SFL and imaged via fluorescence microscopy (see Figure 4.8). However, while these particles were successfully observed in DMSO, we failed to observe an depletion-driven geometric self-assembly. We attempted to transfer a sample of boomerang particles to water to observe hydrophobic assembly, but failed due to particle transfer issues (see Section 3.4.1).

Chapter 5

Conclusions

In this thesis, we studied the fabrication, self-assembly, and dynamical behavior of shape- and chemically-anisotropic colloidal particles. The fabrication of hydrophilic, hydrophobic, and Janus colloidal rods of various sizes and aspect ratios was demonstrated via stop-flow lithography. Image processing algorithms were developed for identifying, locating, and measuring the orientation of colloidal rods in microscopy images, and software was implemented to carry out this analysis and characterize structural and dynamical properties. Single-component particle dynamics were observed via time-series confocal microscopy using particles of various aspect ratios to study the effects of particle geometry on diffusion. The self-assembly of Janus rods was studied using 3D confocal microscopy for particles of various aspect ratios in a number of different solvent conditions to determine the effects of size and attraction strength on the resulting structure. The fabrication of more complex multiple-patch particles with several different geometries was also demonstrated via SFL.

5.1 Future Work

Significant challenges were identified in the areas of particle collection and processing as detailed in Section 3.4.1. These complications may have significantly affected the results of dynamics and self-assembly experiments. It may be possible to reduce these processing complications with the identification of an appropriate non-stick coating. Another possible improvement would be the use of an integrated microfluidic

concentration and cleaning solution to exchange the monomer solution for another solvent.

Once these issues have been solved, a number of interesting studies on the structure and dynamics of suspensions of microfabricated colloids are possible. These include studying self-assembly and dynamics of colloidal suspensions at high concentrations as well as the behavior of two-component suspensions containing a mix of particles with different geometries and functionalities.

It should also be possible to develop image processing algorithms to track particles with more complex geometries. The algorithm developed in Chapter 2 is independent of particle geometry throughout the image cleanup, segmentation, and skeletonization steps. The development of algorithms which could translate the skeletons of other particle geometries into position and orientation information would greatly expand the capabilities of particle tracking.

Appendix A

Rod tracking in Matlab

The results of typical experiments with samples of single-component or Janus rods included both large-area tiled images taken of many particles at a single time, used to study static self-assembly, and movies consisting of many subsequent images in a particular location, taken to study dynamical behavior. Each of these experimental types required the processing of image sets numbering in the hundreds or thousands. The analysis of these images using the algorithm developed above requires the selection of a number of input parameters, such as the thresholding levels and the structuring elements for morphological processing. However, while all the images from a typical experiment could be expected to share the same parameter values, those values might vary considerably for the analysis of different experiments.

To address this, we implemented our algorithm as a set of independent functions which could be carried out manually or called from an automated script. A typical analysis was carried out by selecting one or more test images from the data set; carrying out the various image processing steps on these test images, varying the processing parameters to obtain the best results; and then calling the automation script using the optimized values to process the entire data set. Analysis of test images was generally carried out on a single workstation, while full-dataset processing was carried out on dedicated servers to maximize processing efficiency.

All steps of the analysis were implementing in Matlab [33], making heavy use of functions from the Image Processing Toolbox. The following description summarizes the process of carrying out a manual analysis of test images as a guide to future users.

Listing A.1: Typical sequence of a manual analysis

```
% Load the image.
img = imread('filename.tif');

% If using bandpass cleaning.
clean = bpass(img,lnoise,lobject);

% If using morphological cleaning.
%  top-hat step: radius 50 is greater than rod size.
%  opening step: radius 2 is a good
% size for eliminating small variations.
thstruct = strel('disk',50);
opstruct = strel('disk',2);

% Segmentation step.
watershed_labels = segment(clean, 1);

% Now find backbone pixels.
skeletons = backbones(clean, watershed_labels, 90);

% Finally get the list of positions.
positions = calc_positions(skeletons);
```

A.1 Image Cleanup

Image cleanup is probably the part of the analysis which is most sensitive to parameter selection. Original images of colloidal rod samples from CLSM or FM are often noisy or unevenly illuminated, and these effects vary from experiment to experiment. However, subsequent steps of the analysis assume that their input images will be simple binary images, with white rods and a black background. Choosing the correct parameters to produce such images is a matter of trial and error, and the particular choices must be re-optimized for each new experiment. Two options exist for performing this clean-up: a simple bandpass filter, and a more complex set of morphological operations.

A.1.1 Option 1: Band-Pass

```
clean = bpass(image_array, lnoise, lobject[, threshold])
```

- `image_array`: Matlab array containing image pixels.
- `lnoise`: Characteristic length-scale of noise.
- `lobject`: Characteristic length-scale of object to be tracked (i.e., length of a colloidal rod).
- `threshold`: By default, the last step of this algorithm is to set all negative pixels (generated by the convolution) to be zeros. This parameter may optionally be used to apply a threshold with a different cut-off.

`bpass.m` is from the Blair and Dufrense [21] Matlab implementation of the Crocker and Weeks package for tracking of spherical particles. [19]

A.1.2 Option 2: Morphological Cleanup

`clean = mclean(img, thstruct, opstruct[, threshold])`

- `img`: Matlab array containing image pixels.
- `thstruct`: Matlab structuring element used to carry out the top-hat transform.
- `opstruct`: Matlab structuring element used to carry out the opening and dilation operations.
- `threshold`: By default, the threshold used in this algorithm is selected using the built-in Matlab function `graythresh`, which uses Otsu's algorithm [26]. Here, the user may optionally select a different threshold.

The morphological method for image cleanup is implemented in `mclean.m`, and consists of a top-hat transform, a thresholding, a binary opening, a dilation, and a bitwise AND operation performed in sequence. The function expects the structuring elements for the morphological operations to be passed as arguments, produced by the `strel` function. This is a highly computationally-intensive sequence of operations, but is easily produced using the the functions provided by the Matlab Image Processing Toolkit. The sequence of operations, in Matlab, is illustrated in Listing A.2.

Listing A.2: Morphological image cleanup

```
% Even out illumination using top-hat transform.
th = imtophat(img, thstruct);

% Threshold to produce a binary image.
bw = im2bw(th, graythresh(th));

% Morphological operations: open and dilate to remove noise.
```

```
mo = imdilate(imopen(bw, opstruct), opstruct);

% Produce final image with AND mask.
clean = img;
clean(mo==0) = 0;
```

A.2 Segmentation

`watershed_img = segment(img[, height])`

- `img`: Matlab array containing the image pixels.
- `height`: Maximum height to suppress in h-minima transform. Optional, defaults to 1.

`segment.m` carries out the image segmentation part of the algorithm, and consists of three calls to Matlab built-in functions: `bwdist`, which carries out the distance transform, `imhmin`, which carries out the h-minima transform, and `watershed`, which performs watershed segmentation. While these processes are all computationally intensive, the result is relatively insensitive to processing parameters. The only parameter available is the height of the h-minima transform, which is generally set to 1 to account for single-pixel fluctuations; it is increased only when over-segmentation is observed in the resulting watershed. [28] To observe the resulting watershed segmentation, use the code in Listing A.3.

Listing A.3: Observe watershed segmentation

```
imshow( label2rgb(watershed_img,'jet') );
```

A.3 Skeletonization

`skeletons = backbones(img, watershed_img, percent)`

- `img`: Matlab array containing the image pixels.
- `watershed_img`: Image containing the watershed labels.
- `percent`: Percentile used in the thresholding step.

The generation of the rod skeletons, carried out in `backbones.m`, is also a relatively simple procedure. The results of the watershed segmentation step are used to find the portion of the image which contains each rod, and this is used to generate a new image in which the rod may be analyzed in isolation. The only choice which must be made is the percentile threshold for selecting backbone pixels. This is again a matter of trial and error, but typical values are in the range of 90-95%.

A final image is generated which contains all the backbones, with the pixels belonging to each one having the value of their watershed label. This allows them to be uniquely identified in the following step. The background is assigned again to zero. Observation of these backbones for quality check requires a thresholding step. Observation of all the backbones may be accomplished using the code in Listing A.4, while observing only the backbone with label n may be accomplished using the code in Listing A.5.

Listing A.4: Show all backbones as an image

```
imshow(im2bw(skeletons, 0));
```

Listing A.5: Show only backbone with label n

```
temp=skeletons;
temp(temp~=n)=0;
```

```
imshow(im2bw(skeletons, 0));
```

A.4 Coordinate Calculation

```
positions = calc_positions(skeletons[, cutoff])
```

- `skeletons`: Image containing the rod skeletons.
- `cutoff`: Optional parameter listing a cut-off for ignoring a backbone.

For each individual rod, `calc_positions.m` calculates the positional and orientational coordinates and saves them to the array `positions`. `cutoff` is an optional parameter which allows `calc_positions.m` to ignore backbones which contain under a certain number of pixels, as one last noise-protection step.

`positions` is a 2D Matlab array in which each row represents one backbone, and has the structure:

x	y	z	ϕ	θ

Table A.1: A single row of the `positions` data structure, identifying the coordinates of one rod.

In any 2D image, z and θ are always zero.

A.5 Automated Analysis of Time Series

```
poslist = rod_tseries_bp(imgstack,lnoise,lobject,threshold,height,percent)
```

```
poslist = rod_tseries(imgstack,thstruct,opstruct,threshold,height,percent)
```

A.6 Temporal Tracking

```
tracks = track(xyzs, maxdisp, param)
```

- `xyzs`: An array containing a time-sorted list of particle positions (and, here, orientations).
- `maxdisp`: Maximum allowed displacement of a particle between frames.
- `param`: A data structure containing additional processing parameters.

Frame-to-frame tracking of unique rods to form trajectories was accomplished using a Matlab routine, `track.m`, supplied by Blair and Dufrense [21], implementing the standard algorithm for particle tracking by Crocker and Weeks [19]. `track.m` requires that the data be in a time-sorted format where each row consists of a list of coordinates followed by a frame number, and the frame numbers increase monotonically.

The output, `tracks`, is in a similar format which includes one extra column: a particle "id number" which allows each trajectory to be identified. Rows are ordered so that particle id number increases monotonically, and time increases monotonically within each set of particle rows.

The optional input structure, `param`, contains a variety of settings which alter the behavior of `track`. The only setting important to this analysis is `param.dim`, which tells the program how many columns to use as positional dimensions. Any additional columns will be ignored in the tracking calculation and simply "carried along" when the new array is built; this gives us a place to put our orientation coordinates, which will not be used in the tracking routine.

A.7 Characterization of Rod Suspensions

The location and tracking of colloidal rods within experimental images is not an end in itself, but the first step in determining the characteristics of the suspensions they are used to measure. Data on the position and orientation of all rods within a

suspension is an extremely useful tool, and the values of many dynamical or structural properties may be directly calculated or inferred from this information. While the current work did not proceed so far as to complete a detailed study of all these properties, or implementations of the calculations necessary for such a study, some preliminary work has been done in this area which is worth exploring.

A.7.1 Dynamics

`showmovie(imgstack,tracks)`

`showmovie.m` visualizes the movie from the image stack, plotting a dot-and-bar for each tracked particle on the image to indicate the tracked position and orientation.

```
disps = msd(tracks)
avgs = avg_msd(disps)
```

`msd.m` calculates the mean-square displacement (MSD) for position and orientation for each particle in `tracks`, and returns a data structure `disps` which contains each individual MSD vs time series. `avg_msd.m` takes this structure and averages across particles to produce plots similar to Figure 2.5. Note that this averaging takes place at each individual particle's *own* frame 2, 3, etc. so that the displacement at frame 2 of two particles will be averaged together–even if the second particle did not appear until a later frame. This reduces the total time over which averaging may take place, but improves statistics.

A.7.2 Structure

`result = nearest_neighbors(positions, size)`

```
result = orient_corr(positions)
```

`nearest_neighbors.m` calculates the average number of nearest neighbors for the particles in `positions` within a distance given by `size`. `orient_corr.m` shows how

the dot-product between particle orientations changes with distance.

References

[1] S. C. Glotzer and M. J. Solomon, "Anisotropy of building blocks and their assembly into complex structures," *Nature Materials*, vol. 6, pp. 557–562, 2007.

[2] A. Mohraz and M. J. Solomon, "Direct visualization of colloidal rod assebly by confocal microscopy," *Langmuir*, vol. 21, pp. 5298–5306, 2005.

[3] D. Dendukuri, P. Panda, R. Haghgooie, J. M. Kim, T. A. Hatton, and P. S. Doyle, "Modeling of oxygen-inhibited free radical photpolymerization in a pdms microfluidic device," *Macromolecules*, vol. 41, pp. 8547–8556, 2008.

[4] D. Dendukuri, S. S. Gu, D. C. Pregibon, T. A. Hatton, and P. S. Doyle, "Stop-flow lithography in a microfluidic device," *Lab On a Chip*, vol. 7, pp. 818–828, 2007.

[5] K. M. Zero and R. Pecora, "Rotational and translational diffusion in semidilute solutions of rigid-rod macromolecules," *Macromolecules*, vol. 15, pp. 87–93, 1982.

[6] J. E. G. J. Wijnhoven and W. L. Vos, "Preparation of photonic crystals made of air spheres in titania," *Science*, vol. 281, pp. 802–804, 1998.

[7] G. A. Ozin and S. M. Yang, "The race for the photonic chip: Colloidal crystal assembly in silicon wafers," *Advanced Functional Materials*, vol. 11, pp. 95–104, 2001.

[8] Y. Zhang, S. Wang, M. Eghtedari, M. Motamedi, and N. A. Kotov, "Inverted-colloidal-crystal hydrogel matrices as three-dimensional cell scaffolds," *Advanced Functional Materials*, vol. 15, pp. 725–731, 2005.

[9] H. Yoshida, K. Ito, and N. Ise, "Colloidal crystal growth," *Journal of the Chemical Society, Faraday Transactions*, vol. 87, pp. 371–378, 1991.

[10] S. Wong, V. Kitaev, and G. A. Ozin, "Colloidal crystal films: Advances in universality and perfection," *Journal of the American Chemical Society*, vol. 125, pp. 15589–15598, 2003.

[11] H. N. W. Lekkerkerker, W. C.-K. Poon, P. N. Pusey, A. Stroobants, and P. B. Warren, "Phase behavior of colloid + polymer mixtures," *Europhysics Letters*, vol. 20, pp. 559–564, 1992.

[12] E. Brown, H. M. Jaeger, H. Zhang, N. A. Forman, J. M. DeSimone, B. W. Maynor, and D. E. Betts, "Shear thickening in densly-packed suspensions of spheres and rods confined to a few layers," *Journal of Rheology*, vol. 54, pp. 1023–1046, 2010.

[13] S. H. Chen, Z. L. Wang, J. Ballato, S. H. Foulger, and D. L. Carrol, "Monopod, bipod, tripod and tetrapod gold nanocrystals," *Journal of the American Chemical Society*, vol. 125, pp. 16186–16187, 2003.

[14] L. Manna, D. J. Milliron, A. Meisel, E. C. Scher, and A. P. Alivisatos, "Controlled growth of tetrapod-branched inorganic nanocrystals," *Nature Materials*, vol. 2, pp. 382–385, 2003.

[15] R. F. Shepherd, J. C. Conrad, S. K. Rhodes, D. R. Link, M. Marquez, D. A. Weitz, and J. A. Lewis, "Microfluidic assembly of homogeneous and janus colloid-filled hydrogel granules," *Langmuir*, vol. 22, pp. 205–209, 2006.

[16] H. Zhang, J. K. Nunes, S. E. A. Gratton, K. P. Herlihy, P. D. Pohlhaus, and J. M. DeSimone, "Fabrication of multiphasic and regio-specifically functionalized PRINT®particles of controlled size and shape," *New Journal of Physics*, vol. 11, p. 075018, 2009.

[17] D. Dendukuri, D. C. Pregibon, J. Collins, T. A. Hatton, and P. S. Dolye, "Continuous-flow lithography for high-throughput microparticle synthesis," *Nature Materials*, vol. 5, pp. 365–369, 2006.

[18] A. D. Dinsmore, E. R. Weeks, V. Prasad, A. C. Levitt, and D. A. Weitz, "Three-dimensional confocal microscopy of colloids," *Applied Optics*, vol. 40, pp. 4152–4159, 2001.

[19] J. C. Crocker and D. G. Grier, "Methods of digital video microscopy for colloidal studies," *Journal of Colloid and Interface Science*, vol. 179, pp. 298–310, 1996.

[20] J. C. Crocker and E. R. Weeks, "Particle tracking using idl." `http://www.physics.emory.edu/~weeks/idl/`, October 2010.

[21] D. Blair and E. Dufrense, "The matlab particle tracking repository." `http://physics.georgetown.edu/matlab/`, October 2010.

[22] M. Kilfoil, "Software; particle tracking, feature finding, and microrheology." `http://www.physics.mcgill.ca/~kilfoil/downloads.html`, October 2010.

[23] G. Milne, "The st. andrews tracker (labview)." `http://faculty.washington.edu/gmilne/tracker.htm`, October 2010.

[24] P. Soille, *Morphological Image Analysis: Principles and Applications*. Springer-Verlag, 1999.

[25] D. Mukhija and M. J. Solomon, "Translational rotational dynamics of colloidal rods by direct visualization with confocal microscopy," *Journal of Colloid and Interface Science*, vol. 314, pp. 98–106, 2007.

[26] N. Otsu, "A threshold selection method from gray-level histograms," *IEEE Transactons on Systems, Man and Cybernetics*, vol. 9, pp. 62–66, 1979.

[27] C. Maurer, R. Qi, and V. Raghavan, "A linear time algorithm for computing exact euclidean distance transforms of binary images in arbitrary dimensions," *IEEE Transactions on Pattern Analysis and Machine Intelligence*, vol. 25, pp. 265–270, 2003.

[28] F. Meyer, "Topographic distance and watershed lines," *Signal Processing*, vol. 38, pp. 113–125, 1994.

[29] R. F. Ismagilov, A. D. Stroock, P. J. A. Kenis, G. Whitesides, and H. A. Stone, "Experimental and theoretical scaling laws for transverse diffusive broadening in two-phase laminar flows in microchannels," *Applied Physics Letters*, vol. 76, pp. 2376–2378, 2000.

[30] W. D. Mohr, R. L. Saxton, and C. H. Jepsen, "Mixing in laminar-flow systems," *Industrial and Engineering Chemistry*, vol. 49, pp. 1855–1856, 1957.

[31] D. Dendukuri, T. A. Hatton, and P. Doyle, "Synthesis and self-assembly of amphiphilic polymer microparticles," *Langmuir*, vol. 23, pp. 4669–4674, 2007.

[32] D. C. Pregibon, M. Toner, and P. S. Doyle, "Multifunctional encoded particles for high-throughput biomolecule analysis," *Science*, vol. 315, pp. 1393–1396, 2007.

[33] MathWorks, "MATLAB r2008a," 2008.